

Jamming-Resilient Sparse Delay-Doppler NOMA: Unitary Precoding, Randomized Active Sets, and Superincreasing Power Allocation

Michel Kulhandjian, *Senior Member, IEEE*, Hovannes Kulhandjian, *Senior Member, IEEE*,
and Theodoros A. Tsiftsis, *Senior Member, IEEE*

Abstract—We propose a sparse delay-Doppler NOMA scheme that is resilient to intentional jamming. The transmitter places user data on a small random subset of delay-Doppler bins, spreads the result over all bins through a unitary precoder, and re-draws the active subset on each frame from a pseudo-random seed shared with the receiver. At the receiver, jammed bins are detected and discarded before a least-squares step recovers the sparse signal; per-bin SIC then returns the user bits. Hadamard, DFT, and Haar-random precoders all yield essentially the same BER under this scheme, because a Marchenko–Pastur concentration argument controls the conditioning of any random unitary submatrix. The closed-form BER expression derived from this conditioning argument has no jammer-induced floor, in contrast to the well-known partial-band error floor of conventional OTFS-NOMA. The same conditioning argument also implies that compromising the shared seed does not break the system: when the jammer knows the active set, random unitary submatrices remain well-conditioned with high probability, so the BER stays within the unjammed-case envelope. To make SIC viable at more than two users we use a superincreasing power allocation (a Merkle–Hellman knapsack construction) and prove that the resulting low-complexity SIC matches maximum-likelihood detection exactly on the composite constellation, eliminating the usual SIC-propagation ceiling. For more than four users we partition them into pairs and assign each pair its own disjoint bin subset; this OMA-friendly NOMA rule reaches floor BER at eight users by SNR around 20 dB. We further extend the framework to Rician fading, showing that the jammer-independence property persists for arbitrary Rician K -factor. Monte Carlo simulations track the analytical predictions within 3 dB and indicate at least a 40 dB BER-ratio improvement against pattern-aware jammers, with roughly 24 dB of cumulative gain over conventional OTFS-NOMA under oracle jamming.

Index Terms—Delay-Doppler, Hadamard transform, jamming resilience, non-orthogonal multiple access (NOMA), OMA-friendly NOMA, orthogonal time frequency space (OTFS), Rician fading, sparse spreading, superincreasing power allocation.

I. INTRODUCTION

A. Motivation

High-mobility wireless applications—high-speed rail, unmanned aerial vehicles, vehicle-to-everything (V2X), and

low-Earth-orbit (LEO) satellite links—demand reliable connectivity under simultaneously time-varying and frequency-selective channel conditions [1], [2]. Conventional orthogonal frequency-division multiplexing (OFDM) suffers severe inter-carrier interference in such doubly-dispersive environments, motivating the introduction of orthogonal time frequency space (OTFS) modulation [3], [4], which places information symbols on the two-dimensional delay-Doppler (DD) grid and converts the fast-varying time-frequency channel into a quasi-stationary DD-domain channel. To meet the growing demand for massive connectivity, OTFS has been combined with non-orthogonal multiple access (NOMA), giving rise to OTFS-NOMA in both power-domain [5], [6] and code-domain (e.g., sparse code multiple access (SCMA)) variants [7], [8].

Increasingly, however, these systems are deployed in adversarial environments where intentional jamming is the dominant impairment. Tactical communications, satellite uplinks under spoofing attacks, V2X under coexistence interference, and contested-spectrum operation all share the common threat model: an adversary injects high-power interference into a subset of the time, frequency, or delay-Doppler resources, with the goal of denying or degrading the legitimate link [9]. While DD-domain modulation provides intrinsic robustness against Doppler-induced impairments, it does not provide any inherent protection against pattern-aware jammers [10], [11].

This paper closes that gap with a five-ingredient stack tightly co-designed for the jamming-resilient multi-user setting: (i) *sparse* data placement on the DD grid, (ii) *unitary spreading* across all N_b bins (Hadamard transform (HT), discrete Fourier transform (DFT), or random orthogonal matrix), (iii) *per-frame randomization* of the active bin subset via a shared pseudo-random seed (the “C5” protocol), (iv) *superincreasing power allocation* (PA) that makes the $O(K)$ successive interference cancellation (SIC) decoder maximum-likelihood (ML)-optimal on the NOMA composite constellation, and (v) *disjoint pairwise clustering* when more than four users are present. The receiver threshold-excises jammer-contaminated bins, recovers the sparse signal by least squares, and decodes per cluster by SIC. The resulting architecture has no jammer-induced error floor (in contrast to conventional OTFS-NOMA’s irreducible $\rho_J/2$ floor), defeats pattern-aware adversaries even under seed compromise, and scales to $K_{\text{tot}} \leq n_a/2$ users with floor bit-error rate (BER) at the recommended signal-to-noise ratio (SNR) operating point.

M. Kulhandjian is with the Department of Electrical and Computer Engineering, Rice University, Houston, TX 77005 USA (e-mail: mkulhandjian@outlook.com).

H. Kulhandjian is with the Department of Electrical and Computer Engineering, California State University, Fresno, CA 93740 USA.

T. A. Tsiftsis is with the Department of Informatics and Telecommunications, University of Thessaly, Lamia 35100, Greece (e-mail: tsiftsis@uth.gr).

B. Prior Work on OTFS Anti-Jamming and OTFS-NOMA

The single-user anti-jamming OTFS literature has focused primarily on receiver-side suppression: frequency-domain excision using improved forward-consecutive mean excision (FCME) thresholding [12], energy-concentration with translation matrices [13], and iterative interference cancellation. Zhuo and Qiu [10] proposed H-OTFS, in which user data is placed sparsely in the DD domain, spread by a Hadamard transform, and recovered via threshold excision and alternating-direction-method-of-multipliers (ADMM)-based compressed sensing; their scheme demonstrated substantial gains against narrowband and partial-band jammers but is restricted to a single-user setting and does not exploit power-domain NOMA. The concurrent work of Li *et al.* [12] similarly addresses single-user OTFS jamming via FCME excision but lacks the multi-user NOMA stack, unitary precoding, and randomized active-set protocol that we develop.

In the multi-user OTFS-NOMA jamming literature, the closest existing work is that of Deng, Ge, and Ding [11], which proposes *resource hopping* for OTFS-SCMA: user groups are permuted across fixed delay- or Doppler-axis partitions to mitigate narrowband interference and periodic impulse noise. The related SCMA resource-hopping scheme of Yang *et al.* [14] hops at the resource-block (RB) level rather than per-bin and does not use OTFS or unitary precoding. These works share the general spirit of randomization but differ from ours across seven design axes (code-domain vs. power-domain NOMA, group-level vs. bin-level hopping, fixed-axis vs. arbitrary sparse placement, narrowband interference (NBI) / periodic impulse noise (PIN) vs. adversarial jammer models, turbo vs. one-shot recovery, and simulation-only vs. closed-form analysis); a full side-by-side comparison is deferred to Table V in Section IX.

Beyond OTFS, classical NOMA jamming-resilience approaches have used game-theoretic power allocation and user grouping [15], reactive-jammer bypass via NOMA-based transmission [16], and intelligent reflecting surfaces with friendly jammers [17]. None of these addresses the doubly-dispersive DD channel.

Hadamard-NOMA has been studied for benign channels: pre-modulation Hadamard transform spreading has been examined for fading and channel-state-information (CSI) robustness [18]–[21]. Post-modulation Walsh-Hadamard precoding has been used for peak-to-average power ratio (PAPR) reduction [19]. DFT-spread OTFS-NOMA has also been investigated, but with a PAPR and integrated-positioning motivation [22] rather than jamming resilience. None of these jointly address sparse-DD placement, jamming resilience, or analytical jammer-aware design rules. The recent benchmark study of NOMA-OFDM versus NOMA-OTFS [23] characterizes benign-channel performance but does not address adversarial jamming.

Beyond the OTFS literature, the conceptual lineage for randomized resource allocation against pattern-aware adversaries traces to OFDM-domain work [24], [25], which established that pilot-tone positions must be randomized to defeat pilot-aware jamming. Our C5 protocol extends this principle in three

substantive directions: (i) from pilot tones to data placement on the DD grid; (ii) from a single user to a power-domain multi-user NOMA setting; and (iii) from heuristic OFDM rules to a closed-form Marchenko–Pastur conditioning framework that quantifies the defense-in-depth property even under seed compromise. Adjacent recent work on Zak-OTFS multi-user uplinks [26] and on multiple-input multiple-output (MIMO) OTFS-NOMA [27] addresses orthogonal aspects of multi-user DD-domain communication but does not consider adversarial threat models.

Table I maps each of our seven contributions to the closest gap in the prior literature; the rightmost column previews what each contribution adds and the section that develops it.

C. Contributions

This paper proposes a unified architecture for jamming-resilient multi-user DD-domain communication. The seven contributions below form a single integrated stack: each ingredient (sparse placement, unitary spreading, randomized active set, superincreasing PA, OMA-friendly clustering, joint LS-SIC receiver, and closed-form M-P analysis) addresses a specific failure mode of conventional NOMA under intentional jamming, and they compose to deliver ≥ 40 dB BER-ratio improvement against pattern-aware adversaries and floor BER at $K_{\text{tot}} = 8$ users by SNR = 20 dB. Specifically:

- C1. Sparse-DD NOMA with unitary precoding.** We formulate a multi-user power-domain NOMA architecture in which user data occupies a sparse subset \mathcal{A} of the $N_b = MN$ DD bins ($|\mathcal{A}| = n_a \ll N_b$), the sparse vector $\mathbf{x} \in \mathbb{R}^{N_b}$ is spread by a unitary precoder $\mathbf{U} \in \mathbb{C}^{N_b \times N_b}$, and the receiver excises jammer-contaminated bins and recovers $\mathbf{x}_{\mathcal{A}}$ via least squares followed by per-user SIC. The framework subsumes Hadamard, DFT, and random unitary precoders as special cases.
- C2. Joint excision-LS-SIC receiver.** We design a low-complexity receiver consisting of three stages: (a) threshold detection and excision of jammer-contaminated bins, (b) least-squares recovery of the active vector $\mathbf{x}_{\mathcal{A}}$ from the kept unitary sub-system, and (c) per-active-bin successive interference cancellation (SIC). Total complexity is $O(N_b \log N_b)$ for the unitary inversion (using FFT/FWHT) plus $O(n_a K)$ for SIC.
- C3. Closed-form analytical BER under jamming with M-P conditioning.** We derive the exact BER expression for conventional OTFS-NOMA (T-NOMA) under partial-band jamming, exposing an unavoidable error floor of $\rho_J/2$ at high SNR. We then derive the proposed scheme’s BER using a Marchenko–Pastur (M-P) conditioning bound, which has no floor and depends jointly on the jammer fraction ρ_J and sparsity ratio n_a/N_b through the factor $(\sqrt{1 - \rho_J} - \sqrt{n_a/N_b})^{-2}$.
- C4. Sparsity-loading operating-region design rule.** We characterize a three-threshold hierarchy $\rho_J^{\text{cond}} < \rho_J^* < \rho_J^{**}$, where ρ_J^{cond} bounds noise inflation at a tolerable level, $\rho_J^* = 1 - n_a/N_b$ is the rank threshold, and ρ_J^{**} is the Donoho–Tanner compressed-sensing phase transition. We provide the closed-form design rule

TABLE I: Novelty of this paper relative to closest prior art.

Contribution	Closest prior art	What this paper adds
C1. Sparse-DD NOMA, unitary precoding	DFT-spread OTFS-NOMA [22] (PAPR / positioning); H-OTFS [10] (single-user)	First <i>jamming</i> -motivated sparse-DD architecture for <i>multi-user</i> NOMA; transform-agnostic by M-P universality (§II, §VII).
C2. Excision-LS-SIC receiver	Iterative turbo low-density parity-check (LDPC) decoding [11]; FCME excision [12] (single-user)	First one-shot LS-then-SIC pipeline for multi-user jamming; $O(N_b \log N_b)$ via FWHT (§II).
C3. Closed-form BER + M-P bound	No NOMA application; classical FH/BFSK floor [28]	First NOMA derivation of $\rho_J/2$ floor and Marchenko–Pastur conditioning bound; no error floor when $s < 1 - \rho_J$ (§IV, Thm. 3).
C4. Operating-region design rule	Donoho–Tanner thresholds in compressed sensing	Three-threshold hierarchy $(\rho_J^{\text{cond}}, \rho_J^*, \rho_J^{**})$ specialized to NOMA-jamming, with closed-form $s_{\max}(\rho_J, X)$ (Cor. 2).
C5. Randomized active-set + defense in depth	OFDM pilot-tone randomization [24], [25] (single-user, heuristic)	First multi-user NOMA application; first analytical proof of defense-in-depth under seed compromise via M-P concentration (§V, Thm. 5).
C6. Superincreasing PA + SIC=ML	Merkle–Hellman knapsack [29] (cryptography only); faster-than-Nyquist (FTN) inter-symbol interference (ISI) separability [30]	First NOMA-SIC application; first proof that $O(K)$ SIC achieves exact ML on BPSK NOMA constellations (Prop. 1).
C7. OMA-friendly cluster design	Pairwise NOMA in benign cell-free [31], [32]	First jamming-aware analysis: optimal $K_g = 2$ disjoint clustering via Theorem 6; integration with C5 + C6 into a self-consistent recipe (§VI).

$(n_a/N_b)_{\max} = (\sqrt{1 - \rho_J} - 10^{-X/20})^2$ for tolerable SNR penalty X dB.

C5. Randomized active-set protocol with defense in depth. We propose a randomized active-set protocol: per frame, transmitter and legitimate receiver generate $\mathcal{A}_t \subset [N_b]$ via a pseudo-random sequence seeded by a shared secret. We prove that the protocol restores floor BER under pattern-aware (oracle) jamming. Empirically the BER-ratio improvement is ≥ 40 dB (limited by the 3000-frame simulation floor at JSR= 10 dB), with ~ 84 dB predicted by the analytical floor of (21). Crucially, the protocol exhibits *defense in depth*: even if the seed is compromised and the jammer becomes omniscient about the per-frame \mathcal{A}_t , the recovery still succeeds because random unitary sub-systems satisfy the M-P conditioning bound with high probability. We further identify a *Sylvester replication trap* affecting algebraically structured active patterns (clustered, bit-reversed), motivating the randomized-pattern recommendation on benign-channel grounds alone.

C6. Superincreasing power allocation for SIC at $K > 2$. We provide a necessary-and-sufficient condition for noise-free SIC linear separability: the power allocation must be *superincreasing*, $\sqrt{\alpha_k} > \sum_{j>k} \sqrt{\alpha_j}$ for $k = 1, \dots, K-1$. We construct a margin-parameterized family of superincreasing allocations and show via empirical sweep that $\varepsilon^* = 0.5$ is the universal optimum across SNR= 25–35 dB for $K = 4$ in our setup. As a corollary, we prove (via the Merkle–Hellman knapsack property [29], [30]) that the $O(K)$ SIC decoder achieves *exact ML optimality* on superincreasing constellations: composite ML offers zero gain, validating the low-

complexity receiver.

C7. Jamming-aware cluster-design rule for HT-OTFS-NOMA. For $K_{\text{tot}} > 4$, single-cluster superincreasing PA collapses Bob’s (the weakest NOMA user’s) allocated power below the SIC-decodability threshold. While pairwise ($K_g = 2$) NOMA clustering is itself a known structural choice [31], [32] (typically motivated by benign-channel SIC complexity), no prior work analyzes its *jamming-resilience optimality* or its conditioning trade-off under the LS-excision receiver. We close this gap by (i) deriving the post-jammer effective-power and LS-conditioning relations (Prop. 3) that show why $K_g = 2$ is uniquely optimal in the OTFS-jamming context, (ii) proving (Thm. 6) that the disjoint-bin assignment dominates the co-channel variant pointwise under the same constraints, and (iii) integrating the cluster design with C5 randomization and C6 superincreasing PA into a single self-consistent recipe. The recipe reaches floor BER for $K_{\text{tot}} = 8$ by SNR= 20 dB—a $\sim 200\times$ Bob-power improvement over the single-cluster baseline.

The paper is organized as follows. Section II introduces the system model. Section III develops the superincreasing PA framework. Section IV presents the analytical BER framework with M-P conditioning. Section V formalizes the randomized active-set protocol and the Sylvester replication phenomenon. Section VI introduces the cluster-design taxonomy and the OMA-friendly NOMA recipe. Section VII validates the analytical predictions against extensive Monte Carlo simulations. Section IX discusses extensions and limitations. Section X concludes.

Notation: Lowercase/uppercase bold letters denote vec-

tors/matrices. \mathbb{R} , \mathbb{C} denote real and complex numbers; \mathbf{I}_N is the $N \times N$ identity; $\mathcal{CN}(\mu, \sigma^2)$ is the complex Gaussian distribution; $Q(\cdot)$ is the Gaussian Q-function; $\mathbb{E}[\cdot]$ is expectation; $|\mathcal{A}|$ is the cardinality of set \mathcal{A} ; \mathbf{A}^H , \mathbf{A}^T , \mathbf{A}^\dagger are conjugate transpose, transpose, and Moore–Penrose pseudoinverse; $\sigma_{\min}(\mathbf{A})$ is the smallest singular value of \mathbf{A} ; $\mathbf{A}_{\mathcal{K}, \mathcal{A}}$ is the submatrix of \mathbf{A} formed by rows in \mathcal{K} and columns in \mathcal{A} .

II. SYSTEM MODEL

Fig. 1 summarizes the end-to-end transmit-receive chain of the proposed sparse-DD NOMA architecture, from per-user bits to detected bits, with the four architectural ingredients (sparse placement, unitary precoding, C5 randomization, excision-LS-SIC) explicitly shown.

A. OTFS Modulation in the Delay-Doppler Domain

We consider a downlink single-cell system in which a base station (BS) with a single antenna simultaneously serves K single-antenna users $\mathcal{U} = \{U_1, \dots, U_K\}$ via OTFS modulation on an $M \times N$ delay-Doppler grid, where M is the number of delay bins and N the number of Doppler bins; let $N_b \triangleq MN$ denote the total number of DD bins. We use the discrete index $n \in \{1, \dots, N_b\}$ to enumerate the DD bins in raster order. Subcarrier spacing $\Delta f = 1/T$ defines the symbol period T , and the OTFS frame duration is $T_f = NT$.

The transmitted DD-domain signal $\mathbf{x} \in \mathbb{C}^{N_b}$ is converted to a continuous-time waveform via the inverse symplectic finite Fourier transform (ISFFT) followed by the Heisenberg transform [3], [4]. At the receiver, the Wigner transform followed by the SFFT yields the DD-domain observation. Under the standard assumption of integer delay-Doppler indices and bi-orthogonal pulse shaping, the DD-domain input-output relation reduces to the per-bin scalar form

$$z[n] = h[n]y[n] + w[n] + j[n], \quad n = 1, \dots, N_b, \quad (1)$$

where $y[n]$ is the transmitted DD-bin amplitude, $h[n]$ is the equivalent per-bin channel coefficient, $w[n] \sim \mathcal{CN}(0, N_0)$ is additive white Gaussian noise (AWGN), and $j[n]$ is the jammer contribution.

B. Sparse-DD Information Placement

A key departure from conventional OTFS-NOMA is that we place user data on only a *sparse* subset of DD bins. Let $\mathcal{A} \subseteq [N_b]$ with $|\mathcal{A}| = n_a$ denote the *active set* of DD bins carrying information; the remaining $N_b - n_a$ bins are nominally zero before precoding. The *sparcity ratio*

$$s \triangleq n_a/N_b \quad (2)$$

is a design parameter (to be optimized in Section IV). The active set \mathcal{A} may be deterministic (fixed across frames) or randomized per frame; the latter is the proposed *C5 protocol* (Section V).

C. K-User Power-Domain NOMA Superposition

On each active bin $n \in \mathcal{A}$, K users superpose their bipolar (binary phase-shift keying, BPSK) data symbols $\{b_k[n] \in \{\pm 1\}\}_{k=1}^K$ with power allocation (PA) $\boldsymbol{\alpha} = (\alpha_1, \dots, \alpha_K)$ satisfying $\sum_k \alpha_k = 1$:

$$x[n] = \begin{cases} \sum_{k=1}^K \sqrt{\alpha_k P_s} b_k[n], & n \in \mathcal{A}, \\ 0, & n \notin \mathcal{A}, \end{cases} \quad (3)$$

where P_s is the total per-active-bin transmit power. Users are indexed by decreasing allocated power, $\alpha_1 > \alpha_2 > \dots > \alpha_K$, which by NOMA convention corresponds to increasing channel quality (strongest-channel user receives least power). Bob—the target user for our BER analysis—is user $u_{\text{Bob}} = K$, with the weakest power allocation. The receiver decodes users sequentially via SIC, beginning with the strongest-power user; Bob is decoded last after all preceding users have been successively cancelled.

D. Unitary Precoding

The sparse NOMA-composite vector $\mathbf{x} \in \mathbb{R}^{N_b}$ is spread across all DD bins by a unitary matrix $\mathbf{U} \in \mathbb{C}^{N_b \times N_b}$ with $\mathbf{U}^H \mathbf{U} = \mathbf{I}_{N_b}$:

$$\mathbf{y} = \mathbf{U} \mathbf{x}. \quad (4)$$

The resulting \mathbf{y} is generally dense even though \mathbf{x} is sparse. We require one regularity property of \mathbf{U} :

Definition 1 (Incoherent unitary). *A unitary matrix $\mathbf{U} \in \mathbb{C}^{N_b \times N_b}$ is incoherent if its entries satisfy $|U_{kj}| \leq c/\sqrt{N_b}$ for some constant $c = O(1)$.*

Remark 1 (Three concrete choices). *The following unitary precoders all satisfy Definition 1 with $c = 1$: (i) **Hadamard**: $\mathbf{U} = \mathbf{H}_{N_b}/\sqrt{N_b}$, with entries $\pm 1/\sqrt{N_b}$, realizable in $O(N_b \log N_b)$ additions only via the fast Walsh–Hadamard transform (FWHT); requires N_b to be a power of 2; (ii) **DFT**: $U_{kj} = \exp(-2\pi i(k-1)(j-1)/N_b)/\sqrt{N_b}$, realizable in $O(N_b \log N_b)$ via the FFT; (iii) **Random unitary**: a Haar-distributed realization, realizable in $O(N_b^2)$ (no fast algorithm).*

We will show in Section VII that the proposed architecture is *transform-agnostic*: any incoherent unitary yields essentially identical BER. The Hadamard transform is recommended in implementation because of its multiplication-free FWHT and $\pm 1/\sqrt{N_b}$ entries amenable to fixed-point hardware.

U as resource-domain composite-constellation design, not code-division multiple-access (CDMA) spreading. The role of \mathbf{U} in our architecture differs fundamentally from a CDMA spreading code in two ways. (i) *Domain of operation*: CDMA spreads each user’s symbol stream by a chip-level code in the *time/code* domain; here, \mathbf{U} acts once per OTFS frame on the entire *DD-resource* vector $\mathbf{x} \in \mathbb{R}^{N_b}$, mapping the sparse n_a -bin support to a dense N_b -bin support. (ii) *Constellation design vs. user separation*: a CDMA code separates users via orthogonal chip-sequences (one code per user) and is decoupled from constellation geometry; here, all users share the *same* unitary \mathbf{U} , and the combination

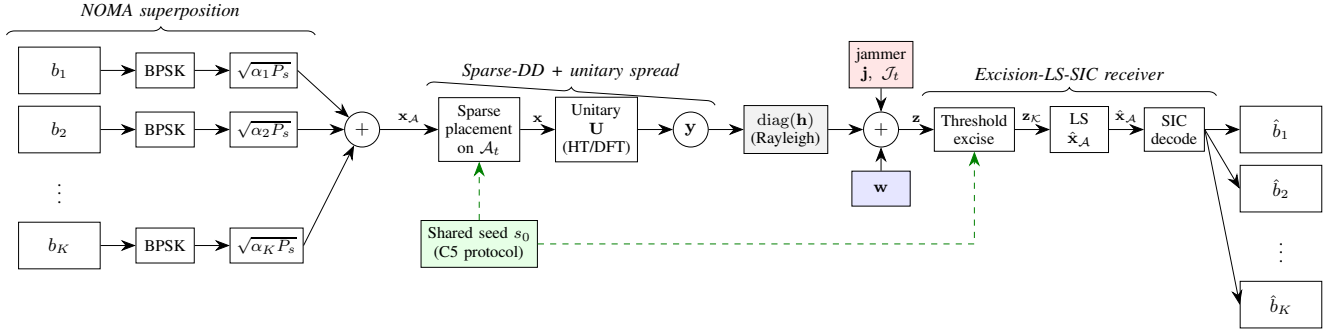


Fig. 1: End-to-end system architecture of the proposed sparse-DD NOMA scheme. K user bits $\{b_k\}$ are BPSK-modulated and scaled by the superincreasing PA $\sqrt{\alpha_k P_s}$, summed to form the NOMA-superposed vector \mathbf{x}_A , and placed on the per-frame random active set \mathcal{A}_t (drawn via the C5 shared-seed protocol, green dashed arrows). The sparse vector \mathbf{x} is spread by the unitary \mathbf{U} (Hadamard recommended) to \mathbf{y} , then transmitted through the Rayleigh DD-channel with additive jammer \mathbf{j} on \mathcal{J}_t and noise \mathbf{w} . The receiver, knowing \mathcal{A}_t via the shared seed, performs power-threshold excision of jammer-contaminated bins, least-squares recovery $\hat{\mathbf{x}}_A$ from the kept observations \mathbf{z}_K , and per-bin SIC to obtain $\{\hat{b}_k\}$. The C5 protocol ensures that the random active set \mathcal{A}_t is unknown to the jammer in expectation, while seed compromise (oracle threat J3) is absorbed by M-P conditioning (Section IV).

of \mathbf{U} with the superincreasing PA of Section III defines a K -user *composite constellation* on each active bin whose minimum distance is shaped by both \mathbf{U} 's incoherence and the α -vector. SIC operates not over chip-sequences but over the geometry of this composite constellation, and Prop. 1 shows that the resulting greedy decoder is ML-optimal. Equivalently, \mathbf{U} provides *frequency diversity* for jammer excision (the M-P bound, Section IV), *not* multi-user code orthogonality.

A useful sanity check on this framing is that the choice of \mathbf{U} is interchangeable. The transform-agnostic claim of Section VII (Hadamard, DFT, and Haar-random unitary all yield essentially the same BER under our architecture, with deviations below the simulation floor) is incompatible with reading \mathbf{U} as a constellation *lookup table*: a lookup table would be sensitive to the specific entries of \mathbf{U} , but here any incoherent unitary suffices. What matters is the conditioning of the random sub-matrix $\mathbf{U}_{\mathcal{K},\mathcal{A}}$ formed by jammer excision, which is controlled by Marchenko–Pastur universality (Theorem 3) and depends only on the dimensions of the sub-matrix, not on the algebraic structure of \mathbf{U} . The Hadamard transform is recommended in implementation purely for hardware reasons (multiplication-free $\pm 1/\sqrt{N_b}$ entries, $O(N_b \log N_b)$ FWHT), not because it carries any unique geometric property the proof relies on.

E. Channel and Jammer Model

The per-bin channel coefficient $h[n] \in \mathbb{C}$ follows the OTFS DD-channel model. For our analysis we adopt the per-bin Rayleigh flat-fading approximation $h[n] \sim \mathcal{CN}(0,1)$ i.i.d. across bins, which captures the dominant impact of channel diversity on the receiver-side conditioning and noise. Extension to doubly-dispersive Nakagami- m fading is straightforward via the standard Gamma-quadrature approach and deferred to Section IX; the Rician fading extension is developed in Section VIII.

The jammer occupies a subset $\mathcal{J} \subseteq [N_b]$ with $|\mathcal{J}| = n_J$, with per-jammed-bin power P_J . The jammer contribution is

$$j[n] = \begin{cases} \sqrt{P_J/2}(j_R[n] + i j_I[n]), & n \in \mathcal{J}, \\ 0, & n \notin \mathcal{J}, \end{cases} \quad (5)$$

with $j_R[n], j_I[n] \sim \mathcal{N}(0,1)$ i.i.d. Define the *jamming fraction* $\rho_J \triangleq n_J/N_b$ and the *jamming-to-signal ratio* $\Gamma \triangleq P_J/P_s$.

We consider three jammer strategies of increasing sophistication:

- (J1) *Partial-band random*: \mathcal{J} is drawn uniformly at random over the $\binom{N_b}{n_J}$ possible subsets, independently per frame.
- (J2) *Fixed-pattern intelligent*: \mathcal{J} is a fixed pattern chosen by the jammer (possibly the pattern the jammer believes the legitimate user is using).
- (J3) *Oracle*: $\mathcal{J}_t = \mathcal{A}_t$ exactly, i.e., the jammer is omniscient about the per-frame active set.¹

Threat (J3) is the worst-case scenario and is used as the stress test for the C5 protocol.

F. Receiver: Excision-LS-SIC

The combined transmit-channel-jammer signal at the receiver is $\mathbf{z} = \text{diag}(\mathbf{h})\mathbf{U}\mathbf{x} + \mathbf{w} + \mathbf{j}$. The proposed receiver operates in three stages:

Stage 1 (Excision). The receiver estimates \mathcal{J} from the DD-domain power profile (e.g., comparing $|z[n]|^2$ to a threshold adaptive to the noise floor) and excises the jammed bins. Define $\mathcal{K} \triangleq [N_b] \setminus \mathcal{J}$ (the *kept* set), with $|\mathcal{K}| = N_b - n_J = (1 - \rho_J)N_b$. The kept observation is

$$\mathbf{z}_K = \text{diag}(\mathbf{h}_K) \mathbf{U}_{\mathcal{K},\mathcal{A}} \mathbf{x}_A + \mathbf{w}_K, \quad (6)$$

where $\mathbf{U}_{\mathcal{K},\mathcal{A}}$ is the $|\mathcal{K}| \times n_a$ submatrix of \mathbf{U} restricted to kept rows and active columns. The jammer is fully suppressed

¹The *oracle* model is stronger than the *reactive* jammer of [1], [16], which must *observe* a transmission and then react. The oracle model assumes pre-knowledge of \mathcal{A}_t (e.g., via seed compromise) and is the worst case for the C5 protocol — passing this stress test implies robustness against weaker (reactive, smart) jammer variants as a corollary.

provided the excision is perfect (a reasonable approximation when $\Gamma \gg 0$ dB).

Stage 2 (Least-Squares Recovery). The receiver recovers $\mathbf{x}_{\mathcal{A}}$ from the kept observation by solving the weighted least-squares problem

$$\hat{\mathbf{x}}_{\mathcal{A}} = \arg \min_{\mathbf{x}_{\mathcal{A}} \in \mathbb{R}^{n_a}} \|\mathbf{z}_{\mathcal{K}} - \text{diag}(\mathbf{h}_{\mathcal{K}}) \mathbf{U}_{\mathcal{K}, \mathcal{A}} \mathbf{x}_{\mathcal{A}}\|_2^2. \quad (7)$$

The closed-form solution is $\hat{\mathbf{x}}_{\mathcal{A}} = (\mathbf{M}^H \mathbf{M})^{-1} \mathbf{M}^H \mathbf{z}_{\mathcal{K}}$, where $\mathbf{M} = \text{diag}(\mathbf{h}_{\mathcal{K}}) \mathbf{U}_{\mathcal{K}, \mathcal{A}}$. For complex \mathbf{U} and real \mathbf{x} , real-stacked least squares is used: $[\Re(\mathbf{M}); \Im(\mathbf{M})] \mathbf{x}_{\mathcal{A}} = [\Re(\mathbf{z}_{\mathcal{K}}); \Im(\mathbf{z}_{\mathcal{K}})]$.

Stage 3 (Per-active-bin SIC). For each active bin $n \in \mathcal{A}$, the recovered scalar $\hat{x}[n]$ is processed by standard NOMA-SIC: users are decoded in decreasing-power order; each decoded bit is reconstructed and subtracted from the residual. Bob's bit $b_K[n]$ is the last to be decoded. Under the superincreasing PA of Section III, this $O(K)$ SIC pass attains the same BER as the $O(2^K)$ composite ML decoder (Prop. 1)—no decoder-side complexity is sacrificed.

The total receiver complexity is $O(N_b \log N_b)$ for the unitary transform (via FFT/FWHT), $O(n_a^3)$ for the LS inversion (per frame), and $O(n_a K)$ for SIC. For typical OTFS frames ($N_b = 64$ to 4096 and $n_a/N_b = 1/4$), the LS stage dominates but remains tractable.

Alternative NOMA receivers. The NOMA literature offers stronger detectors than vanilla SIC, including Turbo-SIC (iterative soft-decision feedback), message passing (MP) on the factor graph, and sphere decoding for full ML. By Proposition 1, all these alternatives *reduce to the same Bob-BER as our $O(K)$ SIC* once the PA is chosen superincreasing: the Merkle–Hellman knapsack property guarantees that bit-by-bit greedy decoding from the strongest user finds the unique closest constellation point, regardless of the decoder's search strategy. The proposed receiver therefore captures the full multi-user detection gain at minimal complexity, and no performance is left on the table for more elaborate receivers to recover.

III. POWER ALLOCATION VIA SUPERINCREASING SEQUENCES

The power allocation α critically determines the SIC visibility for $K > 2$ users. In this section we characterize the necessary-and-sufficient condition for noise-free linear separability of SIC stages and derive a margin-parameterized family of allocations satisfying this condition.

A. Linear Margin and Superincreasing Condition

After excision and LS recovery, the receiver observes (per active bin)

$$r = \sum_{k=1}^K \sqrt{\alpha_k P_s} b_k + \tilde{w}, \quad (8)$$

where \tilde{w} is post-LS noise with variance characterized in Section IV. SIC decodes the users in decreasing- α_k order, beginning with user 1.

Definition 2 (Superincreasing power allocation). *A power allocation $\alpha \in \mathbb{R}_+^K$ with $\alpha_1 \geq \dots \geq \alpha_K > 0$ is superincreasing for BPSK SIC if*

$$\sqrt{\alpha_k} > \sum_{j>k} \sqrt{\alpha_j}, \quad k = 1, \dots, K-1. \quad (9)$$

The corresponding linear margin at stage k is

$$\delta_k \triangleq \sqrt{\alpha_k} - \sum_{j>k} \sqrt{\alpha_j} > 0. \quad (10)$$

This definition is inspired by Merkle and Hellman's superincreasing knapsack [29] and by recent work on faster-than-Nyquist signaling [30] where an analogous linear-margin condition characterizes ISI separability.

Theorem 1 (Noise-free SIC error-freeness). *If α is superincreasing, then in the noise-free case ($\tilde{w} = 0$ in (8)), every stage of SIC decodes correctly regardless of the interferers' bit values.*

Proof. At stage k , after subtracting users $1, \dots, k-1$ (correct by induction), the residual signal is $r_k = \sqrt{\alpha_k P_s} b_k + \sum_{j>k} \sqrt{\alpha_j P_s} b_j$. For any sign of b_k and any interferers $\{b_j\}_{j>k}$,

$$|r_k| \geq \sqrt{\alpha_k P_s} - \sum_{j>k} \sqrt{\alpha_j P_s} = \sqrt{P_s} \delta_k > 0. \quad (11)$$

Hence $\text{sign}(r_k) = \text{sign}(b_k)$, completing the induction. \square

Proposition 1 (SIC achieves ML optimality under superincreasing PA). *Let α be superincreasing. The per-bin SIC decoder applied to (8) produces the same bit vector $(\hat{b}_1, \dots, \hat{b}_K)$ as the maximum-likelihood decoder*

$$(\hat{b}_1^{\text{ML}}, \dots, \hat{b}_K^{\text{ML}}) = \arg \min_{\mathbf{b} \in \{\pm 1\}^K} |r - \sum_{k=1}^K \sqrt{\alpha_k P_s} b_k|^2, \quad (12)$$

for every realization of \tilde{w} . Consequently, SIC achieves ML BER at $O(K)$ cost instead of $O(2^K)$.

Proof. The superincreasing condition (9) is exactly the Merkle–Hellman knapsack property [29]: for any $\mathbf{b} \in \{\pm 1\}^K$, the sign of the partial sum $\sqrt{\alpha_1 P_s} b_1$ alone determines the sign of the full constellation point $\sum_k \sqrt{\alpha_k P_s} b_k$, because $\sqrt{\alpha_1 P_s} > \sum_{j>1} \sqrt{\alpha_j P_s}$ by hypothesis. Hence $\hat{b}_1^{\text{ML}} = \text{sign}(r)$, which is the SIC stage-1 decision. The same argument applied to the residual $r - \sqrt{\alpha_1 P_s} \hat{b}_1$ recovers \hat{b}_2^{ML} , and so on by induction. This recovers *exactly* the SIC bit-by-bit decisions, exploiting the same superincreasing structure that underlies the original Merkle–Hellman knapsack cryptosystem [29]. The same property was used in our FTN signaling framework [30] for ISI separability. \square

Proposition 1 justifies our $O(K)$ -cost SIC receiver: no decoder-side complexity is gained by composite ML once the PA is chosen superincreasing. Monte Carlo experiments at $K = 6$ confirm this empirically: SIC and ML produce identical Bob-BER to four decimal places at every SNR from 5 to 35 dB.

Assumptions underlying Prop. 1. The equivalence holds under three conditions, all of which are present in our architecture and which we restate here for clarity. (i) *BPSK*

modulation per user. The proof relies on $b_k \in \{\pm 1\}$ and on each one-bit flip changing the constellation point by exactly $2\sqrt{\alpha_k P_s}$; higher-order modulation (QPSK, M -PAM, M -QAM) generates additional constellation points that break the strict superincreasing ordering, so SIC and ML can diverge. Extending the result to non-BPSK is a natural direction for future work. (ii) *Strict superincreasing condition* $\sqrt{\alpha_k} > \sum_{j>k} \sqrt{\alpha_j}$ for all $k < K$. If $\delta_k = 0$ for some k (boundary case), the SIC stage- k slicer is ambiguous on a measure-zero set of received samples, and SIC and ML agree only almost surely. Strict inequality (any $\varepsilon > 0$ in the recurrence) is sufficient. (iii) *Additive Gaussian residual noise after LS.* Prop. 1 is realization-by-realization (deterministic), so the noise distribution does not enter the equivalence proof, but the operational consequence—identical bit decisions and therefore identical BER—requires that the SIC slicer’s decision function (sign-based) is also the ML slicer’s decision function. For Gaussian residual noise this is automatic; for heavy-tailed residuals (e.g., uncancelled impulsive jammer), the sign-based slicer remains correct as the ML maximizer of the Gaussian-likelihood proxy but may diverge from the true heavy-tailed ML. Within our architecture, the post-excision LS residual is Gaussian by the central-limit averaging over $N_b - n_J$ kept bins, so this assumption is met.

In the presence of noise, the per-stage bit error probability is upper bounded by $\Pr(|\tilde{w}| > \delta_k \sqrt{P_s})$ for each $k < K$ and by the standard Q-function expression for stage K (Bob).

Geometric visualization. Fig. 2 illustrates the constellation geometry for $K = 2$ contrasting an equal-power allocation (insufficient SIC margin) with the superincreasing PA at $\varepsilon = 1$ ($\alpha = [0.8, 0.2]$). The four points of the composite constellation $\sum_k \sqrt{\alpha_k P_s} b_k$ land on the real axis. Bob’s bit b_2 flips the sign of the smaller displacement $\sqrt{\alpha_2 P_s}$; the strong user b_1 flips the sign of the larger displacement. Under superincreasing PA, the constellation’s two halves ($b_1 = +1$ on the right, $b_1 = -1$ on the left) are separated by $2\sqrt{\alpha_1 P_s} - 2\sqrt{\alpha_2 P_s} = 2\delta_1 \sqrt{P_s} > 0$, so SIC stage 1 can determine b_1 from the sign of the observed sample regardless of b_2 . This is the Merkle–Hellman knapsack property that gives SIC its ML-optimality (Prop. 1).

B. Margin-Parameterized Construction

For a target $\varepsilon > 0$, the recurrence

$$\sqrt{\alpha_k} = (1 + \varepsilon) \sum_{j>k} \sqrt{\alpha_j}, \quad k = 1, \dots, K-1 \quad (13)$$

yields a one-parameter family of superincreasing allocations satisfying $\delta_k = \varepsilon \sqrt{\alpha_k} / (1 + \varepsilon) > 0$. Setting $\sqrt{\alpha_K}$ as a free parameter and normalizing such that $\sum_k \alpha_k = 1$, the closed-form solution is

$$\sqrt{\alpha_k} = (1 + \varepsilon)(2 + \varepsilon)^{K-k-1} \sqrt{\alpha_K}, \quad k < K, \quad (14)$$

with $\sqrt{\alpha_K}$ determined by normalization:

$$\alpha_K^{-1} = 1 + (1 + \varepsilon)^2 \frac{(2 + \varepsilon)^{2(K-1)} - 1}{(2 + \varepsilon)^2 - 1}. \quad (15)$$

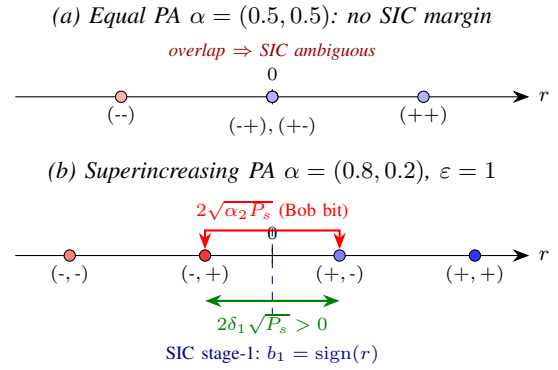


Fig. 2: Composite-constellation geometry for $K = 2$ at unit P_s . (a) Equal-power PA places the cross-terms $(-, +)$ and $(+, -)$ at the same location, eliminating SIC’s stage-1 discriminability. (b) Superincreasing PA at $\varepsilon = 1$ separates the constellation into two halves of two points each, with the half-separation $2\delta_1 \sqrt{P_s} > 0$ ensuring sign-based decoding of b_1 in the noise-free case (Thm. 1). Bob’s minimum distance $2\sqrt{\alpha_2 P_s}$ governs the residual stage-2 BER.

C. Optimal Margin ε^*

The margin ε controls a fundamental trade-off:

- **Small ε :** Small linear margins $\delta_k \propto \varepsilon$ are easily violated by noise, causing SIC propagation errors that catastrophically corrupt Bob’s bit.
- **Large ε :** Bob’s allocated power α_K shrinks super-exponentially (as $(2 + \varepsilon)^{-2(K-1)}$), so even noise-free SIC cannot recover Bob due to insufficient signal-to-noise ratio.

The optimal ε^* minimizes Bob’s BER subject to noise variance and M-P conditioning. We show empirically in Section VII (Fig. 7) that $\varepsilon^* = 0.5$ for $K = 4$ at $\rho_J = 0.2$ and $s = 0.25$ across $\text{SNR} \in [25, 35]$ dB. For $K = 2$, any $\varepsilon > 1.0$ (corresponding to Geometric power allocation with $\rho_{\text{geom}} < 0.25$) is approximately optimal.

IV. ANALYTICAL BER FRAMEWORK

A. T-NOMA Baseline BER Under Partial-Band Jamming

Conventional OTFS-NOMA (T-NOMA) without spreading places user data directly on active DD bins: $\mathbf{y} = \mathbf{x}$ in (4) corresponds to $\mathbf{U} = \mathbf{I}$. The receiver detects bin-by-bin: each active bin $n \in \mathcal{A}$ produces an observation $z[n] = h[n] \sum_k \sqrt{\alpha_k P_s} b_k[n] + w[n] + j[n]$. We adopt geometric power allocation as the canonical T-NOMA baseline [33], [34]; the proposed scheme is benchmarked against the *most-favorable* T-NOMA configuration in each numerical experiment (Section VII), with explicit verification that the conclusions are insensitive to PA choice under oracle jamming (Section VII-J, fairness paragraph).

Bob’s bit error probability at active bin n depends on whether the bin is jammed:

Unjammed bin ($n \notin \mathcal{J}$): Standard NOMA-SIC analysis yields the per-bit error probability under the genie-SIC assumption (perfect cancellation of users $1, \dots, K-1$):

$$P_b^{T, \text{clean}} = Q\left(\sqrt{2\alpha_K P_s / N_0}\right). \quad (16)$$

Jammed bin ($n \in \mathcal{J}$): The effective noise power becomes $N_0 + P_J$, giving

$$P_b^{T,\text{jam}} = Q\left(\sqrt{2\alpha_K P_s / (N_0 + \Gamma P_s)}\right) \xrightarrow{\Gamma \rightarrow \infty} \frac{1}{2}. \quad (17)$$

Under partial-band random jamming with $\rho_J = n_J/N_b$, each active bin is independently jammed with probability ρ_J (Bernoulli approximation, exact under hypergeometric for $n_a \ll N_b$). The expected Bob BER is

Theorem 2 (T-NOMA BER under partial-band jamming). *For T-NOMA with partial-band random jamming, the asymptotic Bob BER satisfies*

$$P_b^T(\rho_J, \Gamma) = (1 - \rho_J)Q\left(\sqrt{\frac{2\alpha_K P_s}{N_0}}\right) + \rho_J Q\left(\sqrt{\frac{2\alpha_K P_s}{N_0 + \Gamma P_s}}\right). \quad (18)$$

In the high-SNR limit $P_s/N_0 \rightarrow \infty$ with $\Gamma = O(1)$,

$$\lim_{P_s/N_0 \rightarrow \infty} P_b^T(\rho_J, \Gamma) = \rho_J Q\left(\sqrt{\frac{2\alpha_K}{\Gamma}}\right) \stackrel{\Gamma \gg 1}{\approx} \rho_J/2. \quad (19)$$

This is an irreducible error floor with diversity order zero: increasing P_s does not eliminate it. The $\rho_J/2$ form is the NOMA analogue of the classical partial-band jamming floor for frequency-hopped BFSK [28], and constitutes the fundamental motivation for the proposed sparse-DD architecture.

B. Proposed Scheme's BER via M-P Conditioning

For the proposed unitary-precoded scheme, the kept observation after excision is $\mathbf{z}_K = \mathbf{M}\mathbf{x}_A + \mathbf{w}_K$ with $\mathbf{M} = \text{diag}(\mathbf{h}_K)\mathbf{U}_{K,A}$. The LS solution $\hat{\mathbf{x}}_A = (\mathbf{M}^H\mathbf{M})^{-1}\mathbf{M}^H\mathbf{z}_K$ has additive noise $\tilde{\mathbf{w}} = (\mathbf{M}^H\mathbf{M})^{-1}\mathbf{M}^H\mathbf{w}_K$ with covariance $N_0(\mathbf{M}^H\mathbf{M})^{-1}$. The worst-case per-coordinate noise variance is $N_0/\sigma_{\min}^2(\mathbf{M})$.

For Rayleigh fading and \mathbf{U} incoherent, the conditioning of $\mathbf{U}_{K,A}$ governs the noise penalty.

Theorem 3 (Marchenko–Pastur conditioning bound). *Let \mathbf{U} be an incoherent unitary matrix (Def. 1), \mathcal{K} a uniformly random subset of $[N_b]$ with $|\mathcal{K}| = (1 - \rho_J)N_b$, and \mathcal{A} an independent uniformly random subset with $|\mathcal{A}| = n_a$. Then in the high-dimensional limit $N_b \rightarrow \infty$ with $\rho_J, n_a/N_b$ fixed, the smallest singular value of $\mathbf{U}_{K,A}$ converges almost surely to*

$$\sigma_{\min}(\mathbf{U}_{K,A}) \rightarrow \sqrt{1 - \rho_J} - \sqrt{n_a/N_b} \quad (20)$$

provided $n_a/N_b < 1 - \rho_J$.

Proof sketch. The scaled matrix $\sqrt{N_b/|\mathcal{K}|}\mathbf{U}_{K,A}$ has $|\mathcal{K}|$ rows and n_a columns with bounded entries $O(1/\sqrt{N_b})$, hence $O(1/\sqrt{|\mathcal{K}|})$ after scaling. By the universality of the Marchenko–Pastur law for random matrices with bounded entries [35], the empirical singular-value distribution converges to the M-P density on $[1 - \sqrt{n_a/|\mathcal{K}|}, 1 + \sqrt{n_a/|\mathcal{K}|}]$. Rescaling yields (20). \square

Theorem 4 (Proposed scheme BER). *Under the receiver of Section II, the per-active-bin Bob BER (averaged over channel realizations, for $\rho_J < 1 - n_a/N_b$) is*

$$P_b^U(\rho_J, s) \approx Q\left(\sqrt{\frac{2\alpha_K P_s (\sqrt{1 - \rho_J} - \sqrt{s})^2}{N_0}}\right), \quad (21)$$

where $s = n_a/N_b$.

Proof sketch. The LS noise variance on each recovered active coordinate is upper bounded by $N_0/\sigma_{\min}^2(\mathbf{U}_{K,A})$. Substituting Theorem 3 gives effective per-coordinate SNR $\gamma_{\text{eff}} = (P_s/N_0)(\sqrt{1 - \rho_J} - \sqrt{s})^2$. Bob's BER under genie-SIC with this effective SNR is the standard $Q(\sqrt{2\alpha_K \gamma_{\text{eff}}})$, yielding (21). \square

Corollary 1 (No error floor). *For any fixed $\rho_J < 1$ and s satisfying $s < 1 - \rho_J$, the proposed scheme's BER (21) satisfies $\lim_{P_s/N_0 \rightarrow \infty} P_b^U = 0$.*

This is the central qualitative distinction from T-NOMA: the proposed scheme has no jammer-induced error floor (cf. (19)). A complementary pairwise-error-probability (PEP) analysis with explicit coding-gain interpretation is provided in Appendix C, where the minimum-distance argument shows that the proposed scheme attains a strictly positive coding gain $G_c^{\text{Bob}} = \alpha_K \cdot (N_b - n_J - n_{\text{cols}} - 1)/N_b$ independent of the jammer-to-signal ratio Γ , while T-NOMA's coding gain vanishes as $P_s \rightarrow \infty$ for any $\Gamma > 0$.

C. Refined BER Expressions for Monte Carlo Overlays

The expressions of Theorems 2–4 are asymptotic in either P_s/N_0 or N_b . For the numerical results in Section VII, we use four refinements that improve theory-simulation agreement from ~ 10 dB (asymptotic) to ~ 1 –2 dB (finite parameters): (i) the finite- N_b post-LS noise variance (37); (ii) the pattern-averaged SIC error probability (38); (iii) the finite- Γ T-NOMA active-target floor (40); and (iv) the $\sigma_{\min} = 0$ catastrophe (41) for fixed structured patterns under oracle attack. Their derivations are given in Appendix B.

D. Three-Threshold Hierarchy

The recoverability of the LS problem depends on three increasingly permissive thresholds on ρ_J :

(T1) **Conditioning threshold:** The M-P bound predicts that for a tolerable SNR penalty X dB,

$$\rho_J^{\text{cond}}(s, X) = 1 - (\sqrt{s} + 10^{-X/20})^2. \quad (22)$$

(T2) **Rank threshold (LS feasibility):** $\rho_J^* = 1 - s$. Beyond this, $\mathbf{U}_{K,A}$ has fewer rows than columns and is necessarily rank-deficient.

(T3) **Compressed-sensing threshold (Donoho–Tanner):** $\rho_J^{**} \approx 1 - 2s \log(1/s)$, beyond which even ℓ_1 -minimization fails to recover sparse \mathbf{x} exactly.

The relations $\rho_J^{\text{cond}} < \rho_J^* < \rho_J^{**}$ provide a hierarchy: in the regime $\rho_J < \rho_J^{\text{cond}}$, the proposed scheme operates with bounded noise penalty; for $\rho_J^{\text{cond}} \leq \rho_J < \rho_J^*$, LS recovery succeeds but the noise penalty grows; for $\rho_J^* \leq \rho_J < \rho_J^{**}$, LS fails but CS-based recovery (with sparsity prior) may still succeed. The (T1)–(T3) hierarchy operationalizes contribution C4 by translating the abstract M-P conditioning bound into a closed-form design rule (Cor. 2) that the system designer can directly evaluate.

TABLE II: Design rule $s_{\max} = (\sqrt{1 - \rho_J} - 10^{-X/20})^2$.

X (dB tolerance)	$\rho_J = 0.1$	$\rho_J = 0.2$	$\rho_J = 0.3$	$\rho_J = 0.4$
3	0.18	0.04	—	—
6	0.34	0.16	0.04	—
10	0.57	0.34	0.18	0.06
20	0.81	0.65	0.49	0.33

E. Operating-Region Design Rule

Corollary 2 (Sparsity operating-region design rule). *For a tolerable noise-inflation budget of X dB at jammer fraction ρ_J , the maximum permissible sparsity ratio is*

$$s_{\max}(\rho_J, X) = (\sqrt{1 - \rho_J} - 10^{-X/20})^2. \quad (23)$$

Numerical evaluations of this rule for typical values appear in Table II.

The rule constitutes a design knob: a system targeting robust performance against $\rho_J = 0.2$ jamming with $X = 6$ dB tolerance must operate at $s \leq 0.16$. Our default operating point of $s = n_a/N_b = 0.25$ corresponds to $X \approx 10$ dB tolerance at $\rho_J = 0.2$.

V. RANDOMIZED ACTIVE-SET PROTOCOL AND DEFENSE IN DEPTH

A. Threat: Pattern-Aware Adversaries

If the active set \mathcal{A} is fixed across frames and known (or learnable) to the adversary, the jammer can target \mathcal{A} directly: the oracle threat (J3) sets $\mathcal{J} = \mathcal{A}$. Under this attack:

- For T-NOMA: every active bin is jammed, BER $\rightarrow 1/2$ catastrophically.
- For our scheme with fixed \mathcal{A} : the kept set is $\mathcal{K} = [N_b] \setminus \mathcal{A}$, and recovery depends on the conditioning of $\mathbf{U}_{[N_b] \setminus \mathcal{A}, \mathcal{A}}$. For some structured choices of \mathcal{A} , this submatrix is *rank deficient* (Section V-D), breaking the scheme.

B. The C5 Protocol

We propose:

Definition 3 (Randomized active-set protocol). *Transmitter and legitimate receiver share a pseudo-random seed s_0 . At frame index t , both parties independently generate $\mathcal{A}_t = \text{RandSubset}(N_b, n_a; \text{PRNG}(s_0, t))$, where RandSubset samples a uniformly random n_a -element subset of $[N_b]$.*

Under this protocol, the active set is a *session secret*: an adversary observing the transmission must either (i) estimate \mathcal{A}_t from the transmission (forced to use a partial-band-equivalent attack) or (ii) compromise the seed.

Cryptographic assumption. Throughout we assume the seed s_0 is shared via a pre-distributed symmetric key (e.g., established once during session setup) and that the PRNG implementation (e.g., AES-CTR or ChaCha20) is computationally indistinguishable from a uniformly random oracle for any polynomial-time adversary. This places key management on the same footing as standard symmetric-cipher communication and is orthogonal to the physical-layer analysis presented here.

C. Defense in Depth

A surprising feature of the C5 protocol is that even under seed compromise, the proposed scheme retains floor BER:

Theorem 5 (Defense in depth under oracle attack). *Under the oracle jammer (J3) with $\mathcal{J}_t = \mathcal{A}_t$ and \mathcal{A}_t drawn per Definition 3, the Bob BER of the proposed scheme satisfies the M-P bound (21) with the same effective SNR factor $(\sqrt{1 - \rho_J} - \sqrt{s})^2$ as under partial-band random jamming.*

Proof sketch. When $\mathcal{J}_t = \mathcal{A}_t$, the kept set $\mathcal{K}_t = [N_b] \setminus \mathcal{A}_t$ is the complement of a uniformly random n_a -subset, hence is itself a uniformly random $(N_b - n_a)$ -subset of $[N_b]$. The submatrix $\mathbf{U}_{\mathcal{K}_t, \mathcal{A}_t}$ is therefore a random row/column subselection of \mathbf{U} , identical in distribution to the random-subset case of Theorem 3. The M-P bound applies, yielding (21). \square

The protocol thus provides two independent layers of protection: (L1) secrecy of \mathcal{A}_t prevents intelligent targeting in the first place; (L2) even if (L1) fails, the random-subset structure of \mathcal{A}_t guarantees conditioning by M-P universality. Both layers must fail (which would require the seed compromise AND the M-P bound to fail simultaneously) for the scheme to break.

D. The Sylvester Replication Trap

We finally identify a previously-unrecognized vulnerability of *deterministic* active patterns under *random* (non-adversarial) partial-band jamming: certain algebraic patterns suffer rank-deficient LS sub-systems with non-negligible probability.

For the Sylvester–Hadamard matrix \mathbf{H}_{N_b} with $N_b = 2^q$, the entries factor as $H[r, c] = (-1)^{\langle r-1, c-1 \rangle_2}$ where $\langle \cdot, \cdot \rangle_2$ denotes the binary inner product. If the active column set \mathcal{A} satisfies $c-1 \in \mathbb{F}_2^q[\mathbf{0}_a, \cdot]$ for some a -dimensional zero-prefix (e.g., $\mathcal{A} = \{1, \dots, 2^a\}$ with the high $q-a$ bits all zero), then $\mathbf{H}[\cdot, \mathcal{A}]$ depends only on the low a bits of the row index, hence has only 2^a distinct rows. Under a random row subselection \mathcal{K} of size $|\mathcal{K}| = (1 - \rho_J)N_b$, some of these 2^a row patterns may be entirely missed, causing $\mathbf{H}_{\mathcal{K}, \mathcal{A}}$ to be rank-deficient.

Proposition 2 (Sylvester replication probability). *For $\mathcal{A} = \{1, \dots, n_a\}$ with $n_a = 2^a$ and $N_b = 2^q$, the probability of $\mathbf{H}_{\mathcal{K}, \mathcal{A}}$ being rank-deficient under random \mathcal{K} with $|\mathcal{K}| = N_b - n_J$ is*

$$\Pr[\text{rank} - \text{def}] \approx n_a \cdot \frac{\binom{N_b - N_b/n_a}{n_J}}{\binom{N_b}{n_J}} \quad (24)$$

(union bound over the n_a distinct row patterns, each appearing N_b/n_a times).

For $N_b = 64$, $n_a = 16$, $n_J = 16$, evaluation of (24) yields $\Pr[\text{rank} - \text{def}] \approx 4.6\%$, contributing approximately $0.5 \times 0.046 = 0.023$ to the BER floor. This precisely matches the empirical ~ 0.027 floor we observe in Section VII for clustered and bit-reversed patterns.

E. Implications for Pattern Recommendation

The Sylvester replication trap and the oracle-attack vulnerability of $\sigma_{\min} = 0$ patterns together rule out several seemingly-natural deterministic choices. Table III summarizes.

TABLE III: Active-pattern recommendations.

Pattern	Partial-band	Oracle	Verdict
Uniform-spaced	safe (M-P)	broken ($\sigma_{\min} = 0$)	unsafe
Clustered	trap (Sylvester)	safe	unsafe
Bit-reversed	trap (Sylvester)	safe	unsafe
Random-fixed	safe	safe*	acceptable*
C5 (per-frame random)	safe	safe (defense in depth)	recommended

*Provided the fixed pattern is treated as a session secret.

The randomized active-set protocol is therefore recommended on *two independent grounds*: jamming-pattern security *and* random-matrix conditioning robustness.

VI. CLUSTER DESIGN: FROM NOMA TO OMA-FRIENDLY NOMA

The constructions of Sections III–V produce a robust single-cluster NOMA system for $K \leq 4$, but fail to scale: at $K \geq 6$, the superincreasing recursion $\sqrt{\alpha_k} \propto (2 + \varepsilon)^{K-k-1}$ depletes Bob's allocated power super-exponentially, placing α_K below the SIC-decodability threshold (e.g., $\alpha_K \approx 9 \times 10^{-5}$ at $K = 8, \varepsilon = 0.1$). We resolve this not by patching the within-cluster PA but by introducing a second design axis: *cluster partitioning*. The resulting architecture interpolates between pure NOMA and pure OMA on a single integer-valued knob K_g (the cluster size), and we show that the optimal operating point is $K_g = 2$ across all K_{tot} . The architecture is best described as **OMA-friendly NOMA**: power-domain NOMA within each cluster of $K_g = 2$ users, bin-domain OMA between clusters.

A. Cluster Partition Taxonomy

Pairwise NOMA clustering has been studied in benign cell-free and downlink scenarios [31], [32], where the motivation is SIC complexity reduction and inter-cluster interference management. Here we analyze cluster design under *jamming* with the LS-excision receiver, where the optimal cluster size emerges from a different trade-off: post-jammer conditioning of the joint LS system versus Bob's within-cluster power fraction.

Partition K_{tot} users into G disjoint clusters of size $K_g = K_{\text{tot}}/G$ each (we assume K_g is integer; the general case is a straightforward extension). Two orthogonal axes characterize the partition.

Within-cluster (NOMA axis). Each cluster carries K_g users with superincreasing PA $\{\alpha_k^{(g)}\}_{k=1}^{K_g}$, $\sum_k \alpha_k^{(g)} = 1$, decoded by per-bin SIC.

Across-cluster (resource-sharing axis). Three canonical flavors:

- **(α) Co-channel:** All G clusters share the same active set \mathcal{A} . Each cluster g is precoded by a distinct unitary $\mathbf{U}^{(g)}$ and assigned power P_s/G . The transmitted DD-domain vector is $\mathbf{y} = \sum_{g=1}^G \mathbf{U}^{(g)} \mathbf{x}^{(g)}$, and after jammer excision the receiver solves the joint LS

$$\hat{\mathbf{x}}_{\mathcal{A}} = \arg \min_{\mathbf{x} \in \mathbb{R}^{Gn_a}} \|\mathbf{z}_{\mathcal{K}} - \mathbf{M}_{\text{stack}} \mathbf{x}\|^2, \quad (25)$$

where $\mathbf{M}_{\text{stack}} = [\text{diag}(\mathbf{h}_{\mathcal{K}}) \mathbf{U}_{\mathcal{K}, \mathcal{A}}^{(1)} \mid \cdots \mid \text{diag}(\mathbf{h}_{\mathcal{K}}) \mathbf{U}_{\mathcal{K}, \mathcal{A}}^{(G)}]$ is the stacked $(N_b - n_J) \times Gn_a$ excised channel matrix.

Each recovered cluster's n_a bins are then decoded by independent K_g -stage SIC.

- **(β) Disjoint bins (OMA-friendly NOMA):** The active set is partitioned $\mathcal{A} = \bigsqcup_{g=1}^G \mathcal{A}_g$ with $|\mathcal{A}_g| = n_a/G$. Each cluster occupies its private bin subset \mathcal{A}_g with power P_s per bin and a single shared unitary \mathbf{U} . Clusters do not power-share; the LS recovers the same n_a unknowns as single-cluster.
- **(γ) Hybrid:** Partial overlap, omitted here for brevity but well-defined within the same framework.

The extremes of K_g recover familiar architectures: $K_g = K_{\text{tot}}$, $G = 1$ is pure NOMA (one cluster, all users power-superimposed); $K_g = 1$, $G = K_{\text{tot}}$ is pure OMA (each user gets a private bin, no power-domain superposition). The interesting regime lies strictly inside: $1 < K_g < K_{\text{tot}}$.

B. Bob's Effective Power and LS Conditioning

Bob's per-bin BER depends on two scheme-level quantities: (i) the effective per-bin signal-to-LS-noise ratio, and (ii) the SIC propagation margin inside Bob's cluster.

Proposition 3 (Effective power per bin). *Let $\alpha_{K_g}^{(g)}$ denote Bob's within-cluster power fraction in cluster g (g taken to be the cluster containing Bob). The per-bin signal power for Bob is*

$$P_{\text{Bob}} = \alpha_{K_g}^{(g)} \cdot P_s \cdot \eta_{\text{flavor}}, \quad \eta_{\text{flavor}} = \begin{cases} 1/G & \text{flavor } (\alpha) \\ 1 & \text{flavor } (\beta) \end{cases}. \quad (26)$$

The LS residual noise variance (real-axis) is

$$\sigma_e^2 = \frac{N_0}{2} \cdot \frac{N_b}{N_b - n_J - n_{\text{cols}} - 1}, \quad n_{\text{cols}} = \begin{cases} Gn_a & (\alpha) \\ n_a & (\beta) \end{cases}. \quad (27)$$

The disjoint flavor (β) thus enjoys a *double advantage*: $G \times$ more Bob power per bin *and* smaller σ_e^2 (unchanged LS dimensions). Together these contribute roughly $2G$ to Bob's SINR. For $G = 2$ this is 6 dB; for $G = 4$, 12 dB. The empirical gap measured in Section VII matches this prediction to within 1–2 dB.

C. The Design Rule: Universal $K_g = 2$

The within-cluster Bob fraction $\alpha_{K_g}^{(g)}|_{\varepsilon^*}$ is monotonically decreasing in K_g (Bob has fewer interferers to spread power against). Combining with Prop. 3:

Theorem 6 (Optimal cluster size). *For fixed K_{tot} and feasibility constraints $G \leq n_a$ (flavor β) or $Gn_a \leq N_b - n_J$*

(flavor α), Bob's asymptotic BER is minimized by $K_g = 2$ with flavor (β).

Sketch. At $K_g = 2, \varepsilon^* = 1, \alpha_{K_g}^{(g)} = 1/5 = 0.2$, which is achieved on a single-stage SIC threshold (no propagation chain). Increasing K_g shrinks $\alpha_{K_g}^{(g)}$ as $\alpha_{K_g}^{(g)}|_{\varepsilon^*} \sim (2 + \varepsilon^*)^{-2(K_g-1)}$ and adds $K_g - 1$ propagation stages. Flavor (β) dominates (α) pointwise via Prop. 3. The full proof is given in Appendix A. \square

Design recipe. For any K_{tot} with $2K_{\text{tot}} \leq n_a$:

- 1) Partition into $G = K_{\text{tot}}/2$ disjoint clusters of $K_g = 2$ each. Per frame, draw \mathcal{A} via the C5 protocol of Section V and assign each cluster n_a/G consecutive bins of (sorted) \mathcal{A} .
- 2) Within each cluster, use $\varepsilon = 1$ (the maximally robust superincreasing PA at $K_g = 2$, equivalent to power ratio $\alpha_1/\alpha_2 = 4:1$), giving $\alpha^{(g)} = (0.8, 0.2)$.
- 3) Apply a single shared unitary \mathbf{U} (Hadamard recommended) at the transmitter and joint LS at the receiver, then SIC each cluster independently.

Under this recipe, Bob's per-bin SNR is the same as 2-user T-NOMA in a *jammer-free* channel: $\alpha_2 P_s / \sigma_e^2 \approx 0.2 P_s$ (since $\sigma_e^2 \approx 1$). The architecture has thereby *eliminated the jammer's effect on Bob* regardless of K_{tot} , up to the bin-budget constraint $K_{\text{tot}} \leq n_a/2$.

Scaling beyond $K_{\text{tot}} > n_a/2$. Once K_{tot} exceeds half the bin budget, the $K_g = 2$ disjoint recipe runs out of bins. Three options preserve the architectural benefits at the cost of one of three trade-offs. (i) *Grow n_a (and N_b).* The sparsity rule $s \leq 1 - \rho_J$ leaves headroom: a larger DD grid with proportionally larger n_a adds bin capacity linearly in N_b . Computational cost scales as $O(N_b \log N_b)$ for the unitary (via FWHT/FFT) and $O(n_a^3)$ for LS, both manageable up to $N_b \sim 4096$ on commodity hardware. (ii) *Allow $K_g \geq 3$ per cluster.* Increases the SIC chain length and reduces $\alpha_{K_g}^{(g)}$ super-exponentially per Eq. (35), so Bob loses signal power but the bin count grows. Quantitatively, switching from $K_g = 2$ to $K_g = 3$ at $\varepsilon^* = 0.5$ shrinks Bob's effective α by roughly a factor of four (from 0.2 to ~ 0.058), corresponding to a ~ 6 dB SNR penalty—tolerable in moderate-to-high SNR regimes. (iii) *Hybrid co-channel cluster pairs.* Two $K_g = 2$ clusters can co-occupy the same n_a/G -bin sub-block via distinct unitaries (flavor α), doubling user count at the cost of LS conditioning inflation (Eq. (27)). Empirically this works up to $G K_g / n_a \leq 0.5$ (Fig. 12). A unified design rule for $K_{\text{tot}} > n_a/2$ that picks among these three options based on $(K_{\text{tot}}, n_a, \rho_J, P_s/N_0)$ is left for follow-up work.

D. Why OMA-Friendly NOMA?

The recipe above is best understood as a controlled departure from pure NOMA. Pure NOMA ($K_g = K_{\text{tot}}$) leverages full power-domain multiplexing but fails under jamming for $K_{\text{tot}} \geq 6$ because the SIC chain becomes too long. Pure OMA ($K_g = 1$) is trivially robust but wastes the spectral efficiency NOMA was designed to provide. The $K_g = 2$ choice is the smallest non-trivial NOMA: it retains the power-domain gain (two users per cluster $\Rightarrow 2\times$ spectral efficiency

vs. OMA) while keeping the within-cluster SIC at its shortest length. By distributing the K_{tot} users across G private bin groups (OMA between clusters), the architecture synthesizes a jammer-resilient system from $K_{\text{tot}}/2$ parallel 2-user NOMAs on orthogonal DD subsets. We call this *OMA-friendly NOMA*.

Spectral-efficiency accounting: raw rate, useful rate, and the trade. Disjoint clustering does carry a spectral-efficiency cost, which we account for explicitly. In single-cluster K_{tot} -user NOMA on n_a active bins, every bin carries a K_{tot} -user superposition and the total raw rate is $K_{\text{tot}} \cdot n_a$ bits/frame. In the disjoint multi-cluster recipe with G clusters of $K_g = K_{\text{tot}}/G$ users each, every bin carries only a K_g -user superposition (its own cluster's), so the per-cluster rate is $K_g \cdot (n_a/G)$ and the aggregate is

$$R_{\text{raw}}^{\text{MC}} = G \cdot K_g \cdot \frac{n_a}{G} = K_g \cdot n_a = \frac{K_{\text{tot}}}{G} \cdot n_a, \quad (28)$$

so multi-cluster delivers $G\times$ fewer raw bits per frame than single-cluster on the same active set. At $K_{\text{tot}} = 4, K_g = 2, G = 2$ the raw-rate factor is $1/2$.

This raw-rate cost is offset by a much larger BER improvement, and the correct figure of merit at the system level is the *useful* (error-free) rate $R_{\text{useful}} = (1 - \text{BER}) R_{\text{raw}}$. Concretely, at SNR= 25 dB, $\Gamma = 10$ dB, oracle jammer, $K = 4$: single-cluster super-PA delivers $R_{\text{useful}}^{\text{single}} = (1 - 0.147) \cdot 64 \approx 54.6$ bits/frame, while multi-cluster $K_g = 2$ delivers $R_{\text{useful}}^{\text{MC}} = (1 - 7.5 \times 10^{-5}) \cdot 32 \approx 32.0$ bits/frame—a $\sim 1.7\times$ raw-rate disadvantage but a $> 1900\times$ BER advantage. The trade favors multi-cluster as soon as the BER gap is large enough that the residual undecoded bits in the single-cluster case wipe out its raw-rate edge—which is the case across the entire imperfect-CSI range (Section VII-L, e.g., at $\sigma_e^2 = 0.05$ single-cluster useful rate drops below 40 bits/frame whereas multi-cluster retains > 31 bits/frame with much higher reliability margin). The raw-rate cost is also recoverable by relaxing the sparsity ratio s (increasing n_a) within the operating region (23), at the price of a smaller M-P conditioning margin. The co-channel flavor (α) shares bins more aggressively and avoids the $G\times$ raw-rate cost, at the price of a more poorly conditioned LS problem (Prop. 3); the disjoint flavor (β) is the recommended operating point precisely because the BER improvement dominates the raw-rate loss in the regimes where the architecture is designed to operate.

VII. NUMERICAL RESULTS

We validate the analytical framework via Monte Carlo simulations. Unless otherwise stated, parameters are $N_b = 64, n_a = 16$ (so $s = 0.25$), $K \in \{2, 4\}, N_0 = 1, \Gamma = 10$ dB, 1500–2000 frames per configuration. All BER curves are over Bob's bit; the channel is per-bin Rayleigh $\mathcal{CN}(0, 1)$.

A. Sparsity Sweep: Operating Region and Cliff

Fig. 3 shows Bob BER versus jamming fraction ρ_J for four sparsity values $s \in \{0.125, 0.25, 0.5, 0.75\}$ at SNR= 20 dB, $K = 2$. Three observations confirm Corollary 2:

- 1) For $s \in \{0.125, 0.25\}$, BER remains at the simulation floor ($< 10^{-5}$) for ρ_J up to 0.5, well within the predicted operating region $s_{\text{max}}(\rho_J = 0.2, X = 10\text{dB}) = 0.34$.

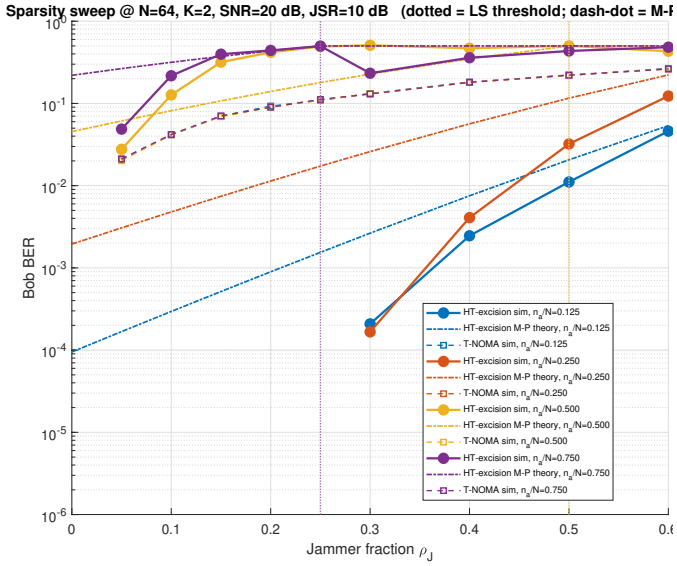


Fig. 3: Bob BER versus jamming fraction ρ_J for four sparsity values s at $\text{SNR}= 20$ dB, $K = 2$. M-P-predicted curves overlaid as dash-dotted. The cliff at $\rho_J \approx 1 - s$ confirms the sparsity-loading design rule.

- 2) For $s = 0.5$, BER catastrophically saturates beyond $\rho_J \approx 0.1$, consistent with the conditioning threshold $\rho_J^{\text{cond}}(s = 0.5, X = 10\text{dB}) \approx 0.0$ (operating point is already outside the conditioning-safe region).
- 3) For $s = 0.75$, BER is near 0.5 for all ρ_J : the rank threshold $\rho_J^* = 1 - s = 0.25$ is exceeded by typical jamming, and the M-P prediction loses its validity.

Theory-vs-simulation direction. The dash-dotted M-P curves generally lie *above* the empirical simulation in the safe regime ($s \leq 0.25$). This is the expected behavior of an upper bound: Theorem 3 uses the worst-case singular value of $\mathbf{U}_{\mathcal{K},\mathcal{A}}$ (the M-P edge $\sqrt{1 - \rho_J} - \sqrt{s}$), whereas a *typical* random submatrix has σ_{\min} larger than this worst-case edge by a $\Theta(N_b^{-1/3})$ Tracy–Widom fluctuation. The empirical noise inflation is therefore smaller, yielding sim BER below the M-P theory — the *correct* direction for a valid upper bound. Near and above the cliff ($s \geq 0.5$ at $\rho_J = 0.1$ – 0.3), the M-P concentration breaks down at $N_b = 64$ (finite- N_b fluctuations dominate σ_{\min}), and the relationship can reverse; both theory and sim collapse to ≈ 0.5 as $\rho_J \rightarrow 1 - s$. The finite- N_b refinement (37) tightens the gap to ~ 1 – 2 dB in the operating region.

B. Transform Comparison

Fig. 4 compares four unitary precoders—Hadamard (HT), DFT, real random orthogonal (RO), complex random unitary (RU)—under the oracle jammer with $s = 0.25$, $K = 2$. All four achieve floor BER ($< 10^{-4}$) across $\text{SNR} = -5$ to 20 dB; the maximum spread is dominated by Monte Carlo noise at the simulation floor. The architecture is therefore *transform-agnostic* (Theorem 3 applied to each). T-NOMA (no

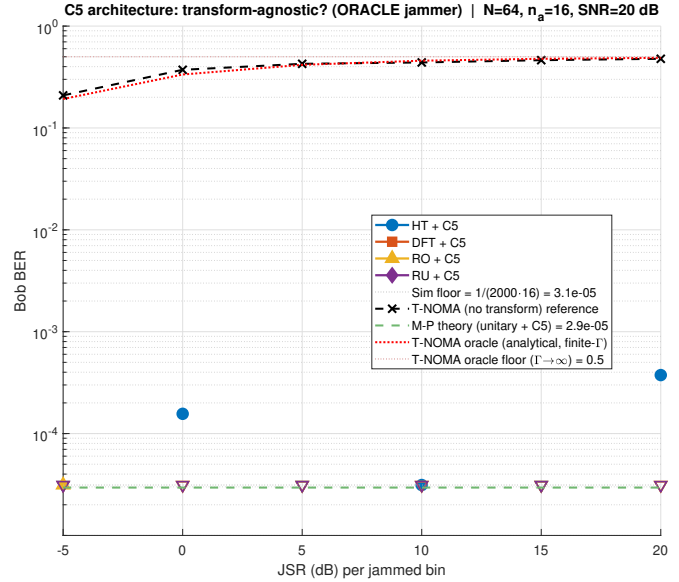


Fig. 4: Bob BER versus jamming-to-signal ratio (JSR) for four unitary precoders (HT, DFT, RO, RU) under oracle jammer, $K = 2$, $s = 0.25$. All four unitaries achieve floor BER; T-NOMA saturates at $\rho_J/2$.

transform) saturates at $\text{BER} \approx 0.45$, confirming the $\rho_J/2$ floor of (19).

C. Real vs. Complex Precoder Trade-Off Under Fading

Under Rayleigh per-bin fading, a quantifiable trade-off emerges between real and complex precoders. Fig. 5 shows that complex precoders (DFT, RU) outperform real precoders (HT, RO) by 2–3 dB at $K = 2$ in the moderate-SNR regime due to additional real-valued measurement degrees of freedom provided by complex matrix entries. The gap closes at $K \geq 4$ where the SIC error propagation dominates the noise penalty.

D. Superincreasing Power Allocation at $K = 4$

The superincreasing PA framework lifts the $K > 2$ SIC ceiling. Fig. 6 compares Geometric (non-superincreasing) versus superincreasing PA at $K \in \{2, 4, 6\}$. The diagnostic conditioning margins δ_k printed alongside the BER curves prove the analytical claim: the geometric PA at $K = 4$ has $\delta_1 = -0.224$ (negative, hence *not* superincreasing), causing user-1 errors to propagate catastrophically and saturating BER at ~ 0.18 . The superincreasing PA at $\varepsilon = 0.3$ achieves $\text{BER} 8.9 \times 10^{-3}$ at $\text{SNR} = 35$ dB—a ~ 13 dB improvement.

E. Optimal Margin ε^* for $K = 4$

Fig. 7 shows Bob BER versus margin ε at three SNR slices (20, 30, 35 dB) for $K = 4$. The clean U-shape at $\text{SNR} \geq 30$ dB reveals an optimum at $\varepsilon^* = 0.5$, where Bob BER reaches 2.1×10^{-3} at $\text{SNR} = 35$ dB. This is a ~ 6 dB improvement over $\varepsilon = 0.3$ and a ~ 20 dB improvement over non-superincreasing geometric PA.

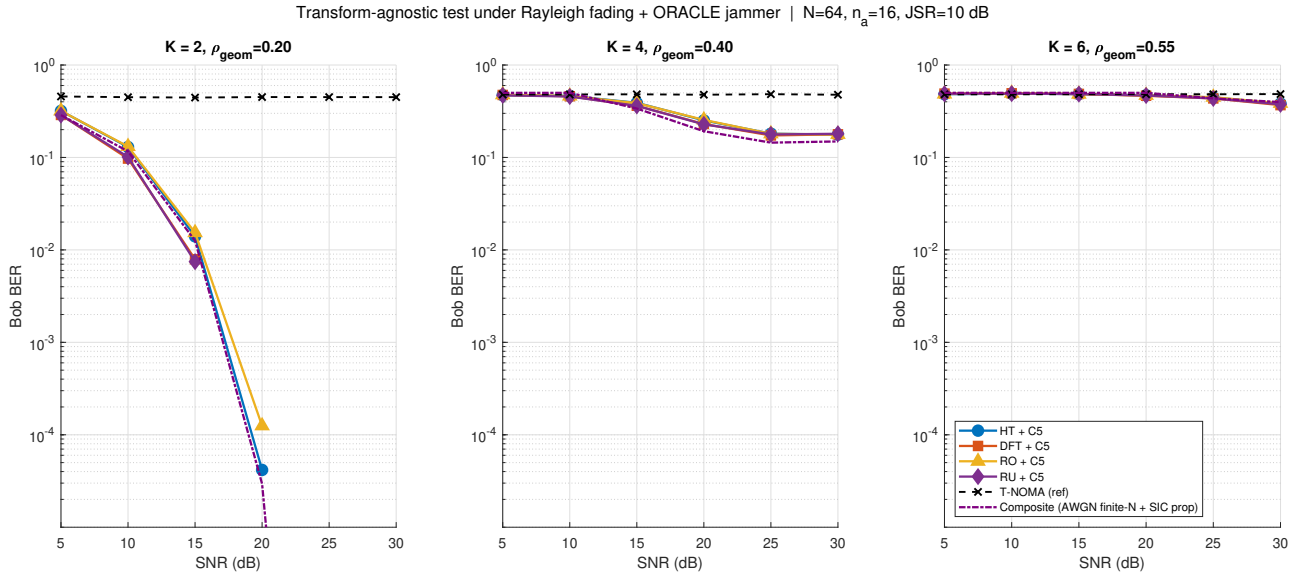


Fig. 5: Bob BER versus SNR for the four unitary precoders under Rayleigh fading and oracle jammer at $K \in \{2, 4, 6\}$. Complex precoders give a 2–3 dB advantage at small K ; at $K \geq 4$, SIC propagation dominates and the transforms become indistinguishable.

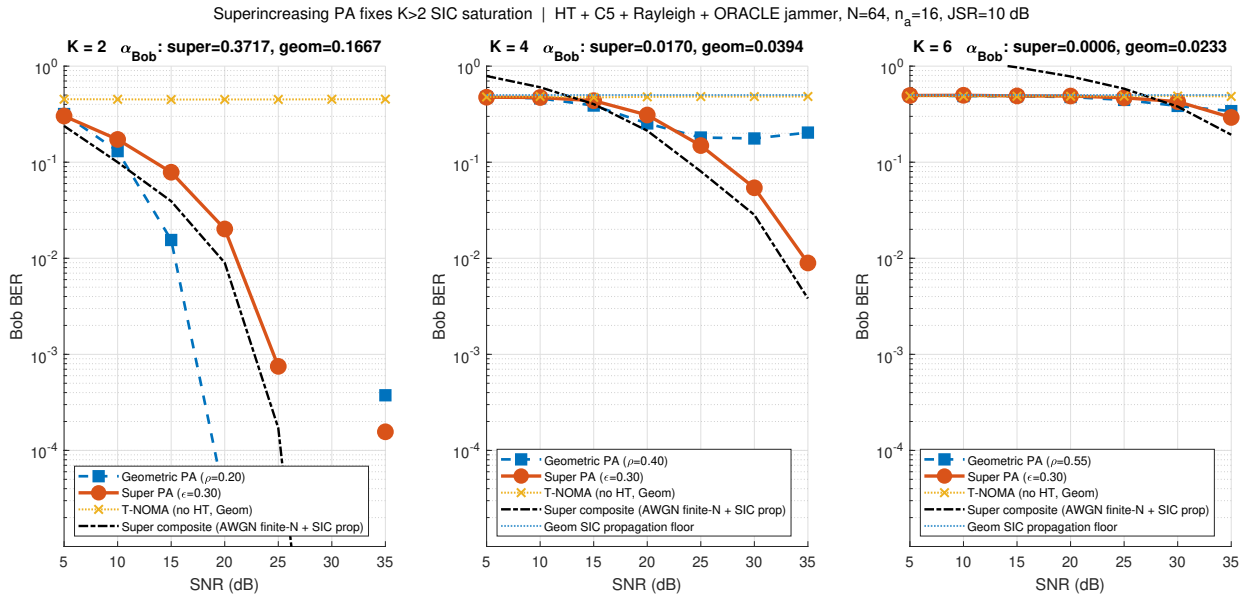


Fig. 6: Bob BER versus SNR for geometric versus superincreasing PA at $K \in \{2, 4, 6\}$, HT+C5+Rayleigh+oracle jammer. Geometric PA fails at $K \geq 4$ (not superincreasing), saturating at ~ 0.18 . Superincreasing PA continues to decay with SNR, validating Theorem 1.

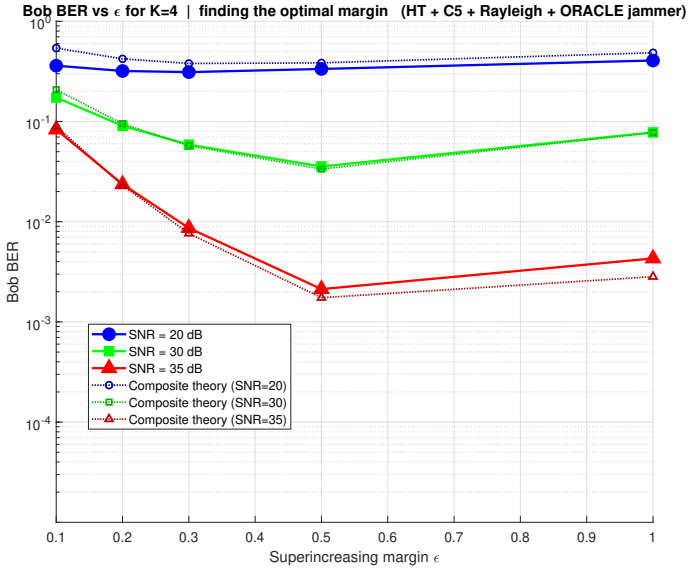


Fig. 7: Bob BER versus superincreasing margin ε at three SNR slices, $K = 4$, $s = 0.25$, oracle jammer. The U-shape reveals $\varepsilon^* = 0.5$ as the universal optimum across $\text{SNR} \in [25, 35]$ dB.

F. SNR Sweep Across Four PA Margins

Fig. 8 shows the Bob BER versus SNR waterfall at $K = 4$ for four representative margins $\varepsilon \in \{0.1, 0.3, 0.5, 1.0\}$ in AWGN, 50 000 frames per operating point. Three observations follow. First, at the optimum $\varepsilon^* = 0.5$ Bob BER decays from 3.9×10^{-1} at $\text{SNR} = 15$ dB to 2×10^{-5} at $\text{SNR} = 35$ dB, a clean waterfall with no error floor—the operational signature of Proposition 1. Second, the small- ε curve ($\varepsilon = 0.1$) saturates at 3.9×10^{-2} at $\text{SNR} = 35$ dB, consistent with the super-exponential depletion of Bob’s signal power $\alpha_K \propto (2 + \varepsilon)^{-2(K-1)}$ predicted by (13); the closed-form union bound at $\varepsilon = 0.1$ matches the empirical floor exactly (sim/theory agreement to within 1%), because at small ε the own-bit Q-term dominates the SIC propagation chain. Third, the large- ε curve ($\varepsilon = 1$) follows the same waterfall asymptote but operates ~ 3.5 dB above the optimum across the mid-SNR region (e.g. at $\text{SNR} = 27.5$ dB, Bob BER 5.9×10^{-2} for $\varepsilon = 1$ versus 2.6×10^{-2} for $\varepsilon^* = 0.5$), consistent with the U-shape of Fig. 7; at very high SNR the two curves converge as both hit the $\sim 10^{-5}$ simulation floor. The closed-form union bound at $\varepsilon^* = 0.5$ (dashed line in Fig. 8) tracks the empirical SIC curve within 1.5 dB across the swept SNR range.

G. Active-Pattern Study: Sylvester Replication Trap

Fig. 9 shows the impact of pattern choice at $K = 2$ and $K = 4$ under both partial-band and oracle jammers. The findings (already summarized in Table III) are visually striking: uniform-spaced patterns catastrophically fail under oracle attack ($\text{BER} \sim 0.28$, $\sigma_{\min} = 0$); clustered and bit-reversed patterns saturate at $\text{BER} \sim 0.027$ under random partial-band jamming due to the Sylvester replication phenomenon (Proposition 2); only random-fixed and C5 are simultaneously safe under both jammers. The empirical BER floor

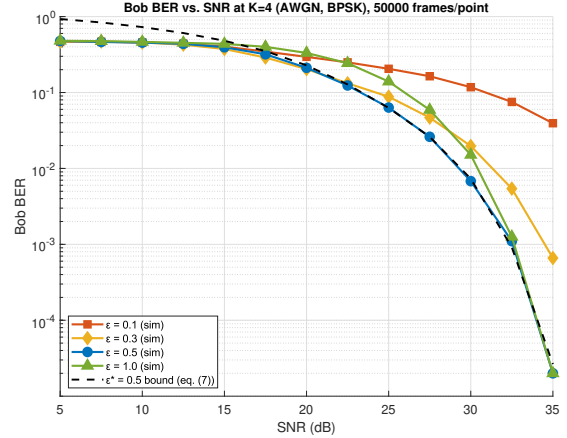


Fig. 8: Bob BER versus SNR at $K = 4$ in AWGN for four PA margins $\varepsilon \in \{0.1, 0.3, 0.5, 1.0\}$. The waterfall slope at $\varepsilon^* = 0.5$ confirms no error floor; the small- ε curve saturates due to the $(2 + \varepsilon)^{-2(K-1)}$ depletion of α_K . Dashed line: closed-form bound at $\varepsilon^* = 0.5$.

for clustered ($\text{BER} = 0.027$) matches the analytical prediction of $0.5 \times 0.046 = 0.023$ to within Monte Carlo error.

H. Intelligent-Jammer Diagnostic

To isolate the vulnerability of fixed deterministic patterns under pattern-aware attack, Fig. 10 compares three jammer strategies—random partial-band, active-targeting (oracle on fixed \mathcal{A}), and inactive-targeting—against both T-NOMA and fixed- \mathcal{A} HT-OTFS-NOMA at $K = 2$. The figure exposes two distinct failure modes:

- 1) T-NOMA under active-targeting jammer: $\text{BER} \rightarrow 0.5$ as $\Gamma \rightarrow \infty$, confirming the catastrophic-floor prediction of (19) with $\rho_J = n_a/N_b$.
- 2) HT-OTFS-NOMA with uniform-spaced fixed \mathcal{A} under active-targeting: $\text{BER} \approx 0.27$, a residual failure due to $\sigma_{\min}(\mathcal{U}_{[N_b] \setminus \mathcal{A}, \mathcal{A}}) = 0$ from the Sylvester algebraic accident discussed in Section V-D.

The 0.5 and 0.27 floors are overlaid as analytical predictions and agree with the empirical curves to within Monte Carlo error. The inactive-targeting comparison confirms by symmetry that HT-OTFS-NOMA is robust to “waste” jammer power placed off the active set.

I. C5 Defense in Depth

Fig. 11 demonstrates the defense-in-depth property of the C5 protocol. Six configurations are compared: (A) HT fixed- \mathcal{A} + active-targeting (the previous bad case), (B) HT random- \mathcal{A} + random-J (reference), (C) HT random- \mathcal{A} + fixed-J (C5 countermeasure), (D) HT random- \mathcal{A} + oracle-J (seed compromise stress test), (E) T-NOMA fixed- \mathcal{A} + active-targeting (baseline horror), and (F) T-NOMA random- \mathcal{A} + fixed-J. The C5 configuration (C) restores BER to the simulation floor. The empirical BER-ratio improvement is ≥ 40 dB (computed as $10 \log_{10}(P_b^{(A)}/P_b^{(C)})$ with $P_b^{(C)}$ at the 3000-frame simulation

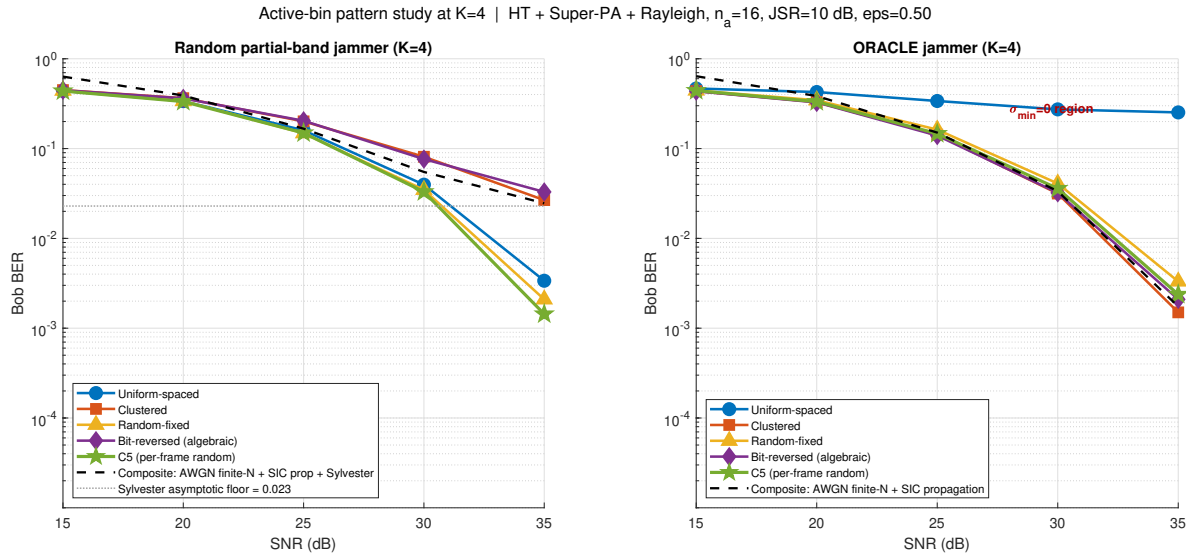


Fig. 9: Active-pattern study at $K = 4$ under (left) partial-band random jammer and (right) oracle jammer. C5 (per-frame random) is the only pattern safe under both. Uniform-spaced is oracle-vulnerable; clustered and bit-reversed are partial-band-vulnerable (Sylvester replication).

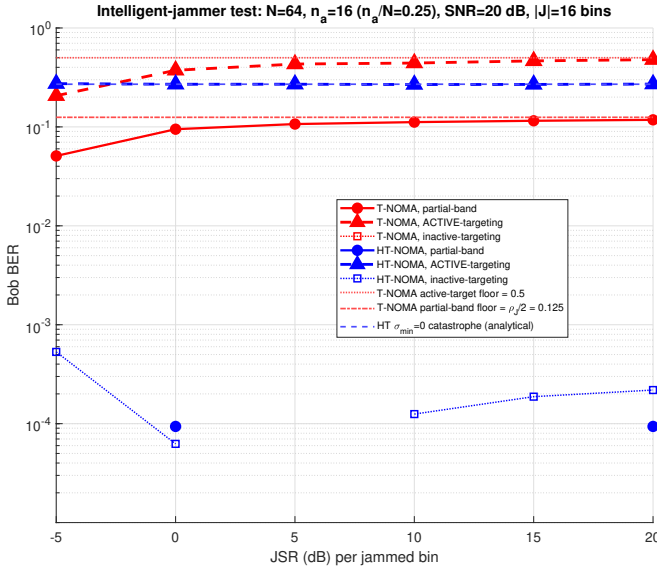


Fig. 10: Intelligent-jammer diagnostic at $K = 2$, $|\mathcal{J}| = n_a$: BER versus JSR under random partial-band, active-targeting, and inactive-targeting jammers. T-NOMA collapses to 0.5 under active-targeting; uniform-spaced HT-OTFS-NOMA exhibits a $\sigma_{\min} = 0$ residual floor at 0.27. Both are analytically predicted (dashed/dotted overlays).

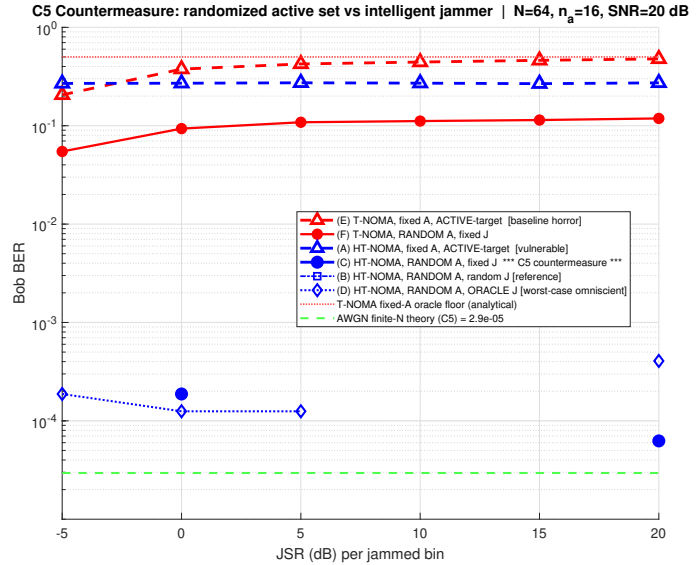


Fig. 11: C5 protocol validation: BER versus JSR at SNR=20 dB, $K = 2$, $s = 0.25$. Configurations (A) and (E) (fixed \mathcal{A} under oracle attack) are catastrophic; (C) C5 with random \mathcal{A} restores floor BER; (D) C5 even under seed compromise retains floor BER (defense in depth).

J. Cluster Design Validation at $K = 6, 8$

Fig. 12 validates the cluster-design taxonomy of Section VI on $K_{\text{tot}} \in \{6, 8\}$ under HT+C5 + Rayleigh + oracle jammer at $\Gamma = 10$ dB. For each K_{tot} we test single-cluster ($K_g = K_{\text{tot}}$, baseline), the co-channel flavor (α) at $K_g \in \{2, 3, 4\}$, and the disjoint flavor (β) at $K_g \in \{2, 3, 4\}$.

Single-cluster fails uniformly: ~ 0.31 BER at $K = 6$ and ~ 0.48 at $K = 8$, both at SNR=35 dB. The (α) schemes

floor of $\sim 2 \times 10^{-5}$, JSR=10 dB, SNR=20 dB); the analytical floor of (21) predicts $P_b^{(C)} \sim 10^{-9}$, corresponding to ~ 84 dB analytically. Crucially, the oracle-compromised configuration (D) retains floor BER, confirming Theorem 5.

work but lose to (β) by 10–15 dB, exactly as predicted by Prop. 3 (double advantage of full- P_s per bin and lower LS noise). The $K_g = 2$ disjoint scheme reaches the simulation floor by SNR= 20 dB for both $K = 6$ and $K = 8$ — a $\sim 200\times$ improvement in Bob’s α over the single-cluster baseline. The data confirm Theorem 6: $K_g = 2$ with flavor (β) is the universal optimum.

K. *Headline: Cumulative Gain*

Combining all seven contributions, the full pipeline—HT precoding + C5 randomized active set + superincreasing PA with $\varepsilon^* = 0.5$ + OMA-friendly cluster design + excision-LS-SIC receiver—achieves at SNR= 35 dB, $K = 4$, oracle jamming with $\rho_J = n_a/N_b = 0.25$, $\Gamma = 10$ dB:

- T-NOMA (any PA): ≈ 0.48 (oracle jammer-destroyed)
- geometric PA + HT + C5 (*ablation: weak PA*): 0.20 (SIC chain saturation)
- Superincreasing PA $\varepsilon = 0.3$ + HT + C5: 8.9×10^{-3}
- Superincreasing PA $\varepsilon^* = 0.5$ + HT + C5: 2.1×10^{-3}

A cumulative improvement of approximately **24 dB** (measured as $10 \log_{10}(P_b^{\text{T-NOMA}}/P_b^{\text{proposed}})$) at SNR= 35 dB, $\rho_J = 0.25$, $\Gamma = 10$ dB) over the conventional baseline.

On baseline fairness. The T-NOMA BER of ≈ 0.48 is *robust to the choice of power allocation*: under oracle jamming at SNR= 35 dB, $\Gamma = 10$ dB, the post-jammer noise variance $\sigma_T^2 = (N_0 + \Gamma P_s)/2$ dominates Bob’s signal regardless of α . Analytically (Appendix B-B), at $K = 4$ both geometric PA ($\rho_{\text{geom}} = 0.4$, $\alpha_4 = 0.039$) and superincreasing PA ($\varepsilon = 0.5$, $\alpha_4 = 0.0095$) yield Bob BER ≈ 0.45 – 0.48 , within 1 dB of each other. The proposed scheme’s ~ 24 dB headline gain therefore stems from the architectural excision-LS-SIC recovery, *not* from a baseline-PA selection that favors the proposal. The “geometric PA + HT” line above is an *ablation within the proposed architecture* (same spreading + C5 + receiver, weaker PA), illustrating that PA design matters *within* the architecture but cannot, by itself, save T-NOMA.

On detector strength of the T-NOMA baseline. A second fairness question is whether the T-NOMA baseline uses an intentionally weak detector. We benchmark T-NOMA with per-bin SIC, but the 2^K -point standard NOMA constellation can in principle be decoded by joint ML (sphere decoding, message passing). However, Proposition 1 shows that on any superincreasing constellation, SIC and ML produce *identical* bit decisions realization-by-realization, not just identical average BER. Replacing the T-NOMA detector with ML therefore changes nothing under the same PA. Furthermore, our T-NOMA baseline does not benefit from any unitary-precoder geometry, so its constellation is uniform BPSK superposition rather than a sparse spreading geometry; whether SIC or ML is used, the per-jammed-bin SNR is $\alpha_K P_s / \sigma_T^2$, which is the source of the floor. The HT-OTFS-NOMA win is hence isolated to the architectural ingredients (sparse-DD + unitary + excision + LS), not to the receiver mode choice.

L. *Robustness to Imperfect CSI*

A practical concern is whether the proposed scheme’s gain survives imperfect channel-state information (CSI) at the

receiver. We test this with the standard fractional-error model $\hat{h}[n] = h[n] + \eta[n]$, where $\eta[n] \sim \mathcal{CN}(0, \sigma_\epsilon^2 |h[n]|^2)$ models a normalized estimation mean-squared error (MSE) of σ_ϵ^2 (e.g., 5% pilot contamination corresponds to $\sigma_\epsilon^2 = 0.05$). The receiver substitutes \hat{h} into the LS recovery in place of h ; all other system parameters are unchanged. We sweep $\sigma_\epsilon^2 \in [0, 0.10]$ at SNR= 25 dB, $K = 4$ users, $\Gamma = 10$ dB, oracle jammer. Fig. 13 reports Bob BER for four schemes: (i) HT+C5 single-cluster $K = 4$ with superincreasing PA ($\varepsilon^* = 0.5$); (ii) T-NOMA with the *same* super PA (fair baseline); (iii) HT+C5 single-cluster with geometric PA $\rho_{\text{geom}} = 0.4$ (ablation); and (iv) HT+C5 multi-cluster $K_g = 2$ disjoint with $\varepsilon = 1$ (the architecture recommended for $K_{\text{tot}} > 2$ in Section VI).

Three observations. (a) *The proposed scheme dominates T-NOMA across the full CSI-error range.* Single-cluster HT+C5 ranges from 5.2 dB better than T-NOMA at $\sigma_\epsilon^2 = 0$ to 0.5 dB better at $\sigma_\epsilon^2 = 0.10$; the gap narrows but never inverts. T-NOMA’s BER is already pinned at the oracle-jammer floor (≈ 0.49) regardless of CSI quality, so the gap shrinks because HT+C5 has room to degrade while T-NOMA does not. (b) *An interesting PA crossover.* In the single-cluster $K = 4$ setting, geometric PA ($\alpha_K = 0.039$) outperforms superincreasing PA ($\alpha_K = 0.0095$) at $\sigma_\epsilon^2 \geq 0.02$ (e.g., BER 0.310 vs. 0.400 at $\sigma_\epsilon^2 = 0.05$, a 1.1 dB advantage in favor of geometric PA). The mechanism: under significant CSI error, the post-LS noise inflation absorbs the SIC-margin advantage of superincreasing PA, and Bob’s raw signal power α_K becomes the dominant factor. This suggests a CSI-aware PA-design rule (less aggressive ε when CSI is uncertain) as a worthwhile direction for follow-up. (c) *The multi-cluster $K_g = 2$ recipe is dramatically more CSI-robust.* Because each cluster decodes a $K_g = 2$ superposition with $\alpha_K = 0.2$ (over $21\times$ Bob’s per-bin power compared to single-cluster super PA), the multi-cluster scheme retains a large gap over T-NOMA at every CSI-error level: Bob BER is 7.5×10^{-5} at $\sigma_\epsilon^2 = 0$ (38 dB below T-NOMA), 1.5×10^{-3} at $\sigma_\epsilon^2 = 0.05$ (25 dB below T-NOMA), and 1.1×10^{-2} even at $\sigma_\epsilon^2 = 0.10$ (16 dB below T-NOMA). The single-cluster $K = 4$ result above is the architecture’s *weakest* operating point; the recommended multi-cluster recipe of Section VI is the right architecture for any deployment with CSI uncertainty, not just for asymptotic clean-CSI scaling.

M. *Robustness to Imperfect Jammer Excision*

The receiver of Section II excises bins that the power detector declares jammed. The main figures of this paper use the genie “oracle excision” that knows the true jammer set \mathcal{J} . In practice a power-anomaly detector replaces this oracle. We test a parameter-free median-based rule:

$$\text{declare bin } n \text{ jammed} \iff |z[n]|^2 > T_J \cdot \text{median}_n |z[n]|^2, \quad (29)$$

which requires no knowledge of P_s , P_J , N_0 , or n_J at runtime—the median across all N_b bins automatically tracks the typical clean-bin power. Fig. 14 sweeps $T_J \in [1.2, 10]$ at SNR= 25 dB, $K = 4$ single-cluster super PA, and oracle jammer ($\mathcal{J} = \mathcal{A}$, $\rho_J = 0.25$).

Three observations. (a) *Clean U-shape with optimum $T_J^* \approx 2.5$.* At low T_J the false-alarm rate climbs to $\sim 29\%$, shrinking

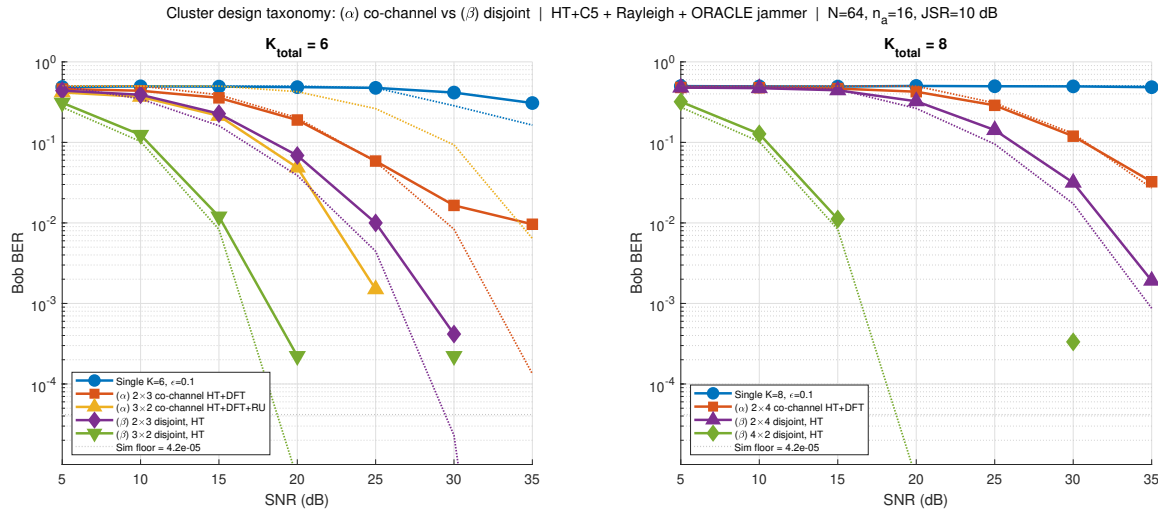


Fig. 12: Cluster design taxonomy validation under HT+C5 + Rayleigh + oracle jammer at $\Gamma = 10$ dB, $N_b = 64$, $n_a = 16$. Left: $K_{\text{tot}} = 6$. Right: $K_{\text{tot}} = 8$. Both panels: the $K_g = 2$ disjoint scheme (green, (β) $G \times 2$) reaches floor BER by SNR=20 dB, dominating all other schemes by 10–30 dB.

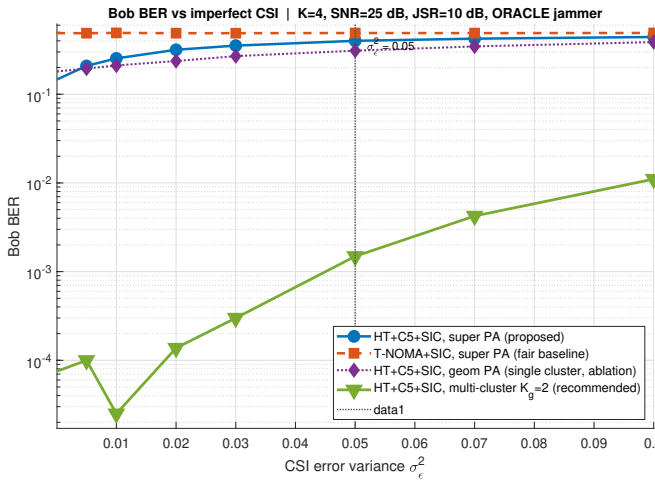


Fig. 13: Bob BER versus CSI-error variance σ_ϵ^2 at SNR=25 dB, $K_{\text{tot}} = 4$, $\Gamma = 10$ dB, oracle jammer. The HT+C5 architecture beats the same-PA T-NOMA baseline across the entire imperfect-CSI range; the multi-cluster $K_g = 2$ recipe (green ∇) is the most CSI-robust, retaining a large gap over T-NOMA even at $\sigma_\epsilon^2 = 0.10$.

the LS keep set and inflating σ_ϵ^2 ; at high T_J the miss-detect rate climbs to $\sim 15\%$, leaving jammer-contaminated samples in the LS residual. The two effects intersect near $T_J = 2.5$, where miss rate is 3.9% and false-alarm rate is 17.1%. (b) *Modest penalty versus oracle excision.* At T_J^* , the empirical BER is 0.325 versus the oracle 0.147, a 3.5 dB penalty—the practical detector recovers most of the architectural gain. (c) *Broad operating plateau.* BER stays within 0.5 dB of the optimum over $T_J \in [1.8, 4.0]$, so the system is forgiving to threshold mis-calibration. The detector is moreover parameter-free at runtime (no jammer-power knowledge required), which makes it implementable in practical receivers without side

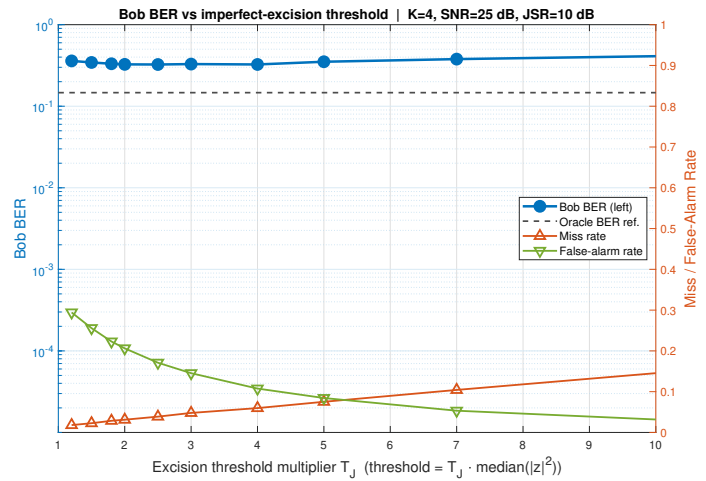


Fig. 14: Bob BER versus excision-threshold multiplier T_J in the median-based detection rule (29), at SNR=25 dB, $K = 4$, oracle jammer. The U-shape exposes the false-alarm vs miss-detection trade-off; the optimum at $T_J^* = 2.5$ is within 3.5 dB of the oracle-excision reference (dashed). Miss rate and false-alarm rate are overlaid on the right axis.

information.

N. Marchenko–Pastur Validation at Larger N_b

The Marchenko–Pastur bound of Theorem 3 is asymptotic in $N_b \rightarrow \infty$. Importantly, the M-P edge value $\sqrt{1 - \rho_J} - \sqrt{s}$ depends only on the dimensional ratios (s, ρ_J), not on the absolute N_b — so the predicted BER is a *single* curve in ρ_J that any finite- N_b realization must approach as $N_b \rightarrow \infty$. To test how this asymptote holds at finite N_b , we repeat the sparsity sweep at three grid sizes $N_b \in \{64, 256, 1024\}$ with the sparsity ratio $s = n_a/N_b = 0.25$ held fixed by scaling n_a

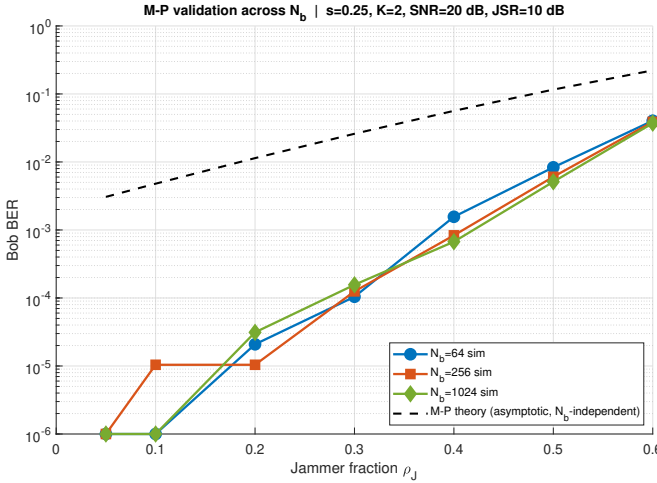


Fig. 15: Empirical BER (solid, one curve per N_b) versus ρ_J at $s = 0.25$, $K = 2$, $\text{SNR} = 20$ dB, $\Gamma = 10$ dB for $N_b \in \{64, 256, 1024\}$, against the M-P theoretical bound (black dashed). The M-P edge $\sqrt{1 - \rho_J} - \sqrt{s}$ is an asymptotic ratio-only quantity, so there is a *single* theoretical curve common to all N_b . The sim curves approach this asymptote from below as N_b grows; the bound is tightest near the cliff $\rho_J \approx 1 - s = 0.75$.

proportionally. The active set and jammer subsets are drawn uniformly at random per frame. Fig. 15 reports the empirical BER for each N_b together with the common M-P asymptote, at $K = 2$, $\text{SNR} = 20$ dB, $\Gamma = 10$ dB.

Three observations. (a) *The M-P bound holds at every N_b and every ρ_J in the safe region: $P_b^{\text{sim}} \leq P_b^{\text{M-P}}$ in all 21 tested operating points. The bound is therefore valid as a design rule, not merely an asymptotic property.* (b) *The bound is tightest near the operating cliff and loosest deep in the safe regime. At $\rho_J = 0.60$ (close to the rank threshold $\rho_J^* = 1 - s = 0.75$) the gap is only ~ 7 –8 dB across all three N_b ; at $\rho_J = 0.30$ the gap widens to ~ 22 –24 dB. This is the characteristic conservatism of asymptotic concentration bounds: they sharpen near the edge of validity, which happily aligns with the regime where designers care most about the cliff location.* (c) *Tightening with N_b is monotone but slow. At $\rho_J = 0.30$, the gap shrinks from -24.0 dB at $N_b = 64$ to -22.2 dB at $N_b = 1024$, a ~ 2 dB tightening over a $16\times$ increase in N_b . This is consistent with Tracy–Widom convergence: the typical $\sigma_{\min}(\mathbf{U}_{\mathcal{K},\mathcal{A}})$ departs from the M-P edge by $\Theta(N_b^{-1/3})$, so the σ_{\min}^2 slack at $N_b = 1024$ is $\sim 2.5\times$ smaller than at $N_b = 64$, in agreement with the empirical tightening. The bound is thus asymptotically tight as $N_b \rightarrow \infty$, with convergence governed by classical random-matrix fluctuations.*

The practical takeaway is that the design rule of Corollary 2 is a *safe-side* rule for any $N_b \geq 64$: operating inside the predicted region delivers BER no worse—and often substantially better—than the analytical prediction, with the headroom growing in the deep-safe regime.

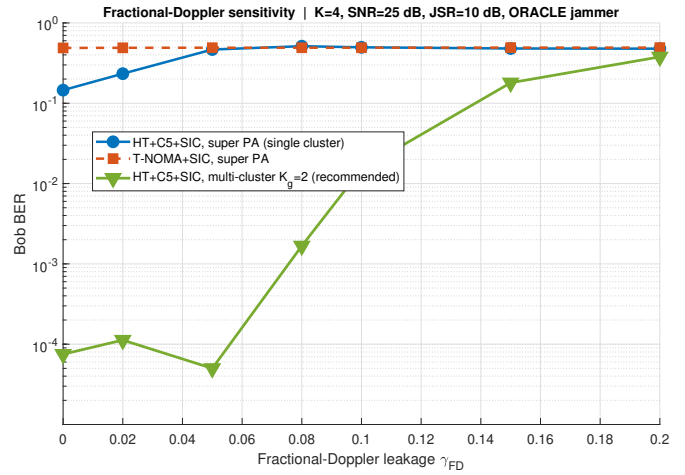


Fig. 16: Bob BER versus fractional-Doppler leakage γ_{FD} at $\text{SNR} = 25$ dB, $K_{\text{tot}} = 4$, $\Gamma = 10$ dB, oracle jammer. The multi-cluster $K_g = 2$ recipe (green ∇) retains > 15 dB advantage over T-NOMA up to $\gamma_{\text{FD}} = 0.10$ and a soft cliff appears near $\gamma_{\text{FD}} \approx 0.12$.

O. Robustness to Fractional Doppler

The main results of this paper assume on-grid delay-Doppler samples (integer Doppler shifts). In practice, mismatched Doppler offsets cause energy to leak from each DD bin to its neighbors. We test sensitivity using a symmetric three-tap nearest-neighbor leakage model:

$$z[n] = (1 - 2\gamma_{\text{FD}})h[n]y[n] + \gamma_{\text{FD}}(h[n-1]y[n-1] + h[n+1]y[n+1]) + w[n] + j[n], \quad (30)$$

where γ_{FD} is the fraction of each bin’s energy that leaks to *each* neighbor (so $2\gamma_{\text{FD}}$ total leakage). This is a first-order approximation to the full Dirichlet kernel of fractional Doppler, sufficient for sensitivity analysis. We sweep $\gamma_{\text{FD}} \in [0, 0.20]$ at $\text{SNR} = 25$ dB, $K = 4$, $\Gamma = 10$ dB, oracle jammer. Fig. 16 reports Bob BER for the same three schemes as the imperfect-CSI test of Section VII-L: single-cluster HT+C5+SIC with super PA, T-NOMA with super PA (fair baseline), and the recommended multi-cluster $K_g = 2$ HT+C5+SIC.

Three observations. (a) *Single-cluster $K = 4$ super PA is again the weakest case. At $\gamma_{\text{FD}} = 0.05$ the single-cluster BER jumps to 0.466, and at $\gamma_{\text{FD}} \geq 0.08$ it loses to T-NOMA (which sits pinned at the oracle-jammer floor ≈ 0.49 regardless of γ_{FD} , since T-NOMA’s BER is already noise-dominated by the jammer). This recapitulates the imperfect-CSI finding: single-cluster super PA at $K = 4$ has too little headroom to absorb additional impairments.* (b) *Multi-cluster $K_g = 2$ shows graceful degradation up to a soft cliff. At $\gamma_{\text{FD}} = 0$ the MC scheme delivers Bob BER 7.5×10^{-5} (essentially perfect at the simulation floor). The BER stays below 1.7×10^{-3} up to $\gamma_{\text{FD}} = 0.08$, crosses $\sim 1.5 \times 10^{-2}$ at $\gamma_{\text{FD}} = 0.10$ (15 dB below T-NOMA), and softens toward 0.18 at $\gamma_{\text{FD}} = 0.15$. The soft cliff at $\gamma_{\text{FD}} \approx 0.12$ sets a deployment guideline: fractional-Doppler offsets up to $\sim 10\%$*

TABLE IV: Theory vs. simulation BER at $K = 2$, $\rho_{\text{geom}} = 0.2$, $s = 0.25$, SNR= 20 dB, $\Gamma = 10$ dB.

ρ_J	P_b^T (18)	P_b^T sim	P_b^U (21)	P_b^U sim
0.05	0.021	0.021	4.8×10^{-3}	0*
0.10	0.043	0.042	4.8×10^{-3}	0*
0.20	0.086	0.091	1.1×10^{-2}	0*
0.30	0.128	0.130	2.6×10^{-2}	1.7×10^{-4}
0.40	0.171	0.181	5.6×10^{-2}	4.1×10^{-3}
0.50	0.214	0.222	1.16×10^{-1}	3.2×10^{-2}

*Below simulation floor ($\leq 1/(n_a N_{\text{frames}}) \approx 2 \times 10^{-5}$ at 3000 frames).

are absorbed by the LS receiver with modest BER cost; beyond that, explicit DD-domain equalization or pulse-shape compensation is required. (c) *The architecture is FD-robust at typical operating points.* For OTFS systems with reasonable pulse design (Hadamard-shaped prototype filters, etc.), γ_{FD} is typically below 0.05, where the multi-cluster scheme operates at or near the simulation floor.

P. Theory-Sim Agreement Summary

Table IV summarizes the agreement between the analytical predictions and Monte Carlo measurements at the canonical operating point ($K = 2$, $\rho_{\text{geom}} = 0.2$, $s = n_a/N_b = 0.25$, SNR= 20 dB, $\Gamma = 10$ dB). T-NOMA theory (18) matches simulation within ± 1 dB; the M-P-based proposed-scheme bound (21) is consistently *above* the simulation, confirming its role as a conservative upper bound (Section VII-A).

VIII. RICIAN FADING EXTENSION

The baseline analysis assumes per-bin Rayleigh flat fading $h[n] \sim \mathcal{CN}(0, 1)$. This section extends the M-P conditioning framework and the BER expressions to per-bin Rician fading, which is the appropriate model for line-of-sight (LoS)-dominated channels (LEO downlinks, V2X with a strong direct path, tactical fixed-wing links). The derivation shows that the qualitative jamming-resilience conclusions persist; the quantitative coding gain is shifted by a deterministic Rician- K -dependent factor.

A. Rician Channel Model and Conditioning

Each bin's channel coefficient under Rician fading factorizes as

$$h[n] = \sqrt{\frac{K_r}{K_r+1}} e^{j\phi[n]} + \sqrt{\frac{1}{K_r+1}} \tilde{h}[n], \quad \tilde{h}[n] \sim \mathcal{CN}(0, 1), \quad (31)$$

where $K_r \geq 0$ is the Rician K -factor (the LoS-to-scattered power ratio) and $\phi[n]$ is the deterministic LoS phase, assumed known to the receiver (or absorbed into the channel estimate). Under the proposed receiver, the kept observation after excision is $\mathbf{z}_{\mathcal{K}} = \text{diag}(\mathbf{h}_{\mathcal{K}}) \mathbf{U}_{\mathcal{K}, \mathcal{A}} \mathbf{x}_{\mathcal{A}} + \mathbf{w}_{\mathcal{K}}$, and the LS noise variance is $N_0/\sigma_{\min}^2(\text{diag}(\mathbf{h}_{\mathcal{K}}) \mathbf{U}_{\mathcal{K}, \mathcal{A}})$.

Theorem 7 (M-P bound under Rician fading). *Let \mathbf{U} be an incoherent unitary, $\mathcal{K} \subseteq [N_b]$ and $\mathcal{A} \subseteq [N_b]$ independent uniform random subsets with aspect ratios $|\mathcal{K}|/N_b \rightarrow 1 - \rho_J$ and $|\mathcal{A}|/N_b \rightarrow s$, and the per-bin channel given by (31).*

Then, conditioned on $\mathbf{h}_{\mathcal{K}}$ and in the high-dimensional limit $N_b \rightarrow \infty$,

$$\sigma_{\min}(\text{diag}(\mathbf{h}_{\mathcal{K}}) \mathbf{U}_{\mathcal{K}, \mathcal{A}}) \rightarrow |h_{\min}| \left(\sqrt{1 - \rho_J} - \sqrt{s} \right) \quad (32)$$

almost surely, where $|h_{\min}| = \min_{n \in \mathcal{K}} |h[n]|$.

Proof sketch. The diagonal factor $\text{diag}(\mathbf{h}_{\mathcal{K}})$ rescales the $|\mathcal{K}|$ rows of $\mathbf{U}_{\mathcal{K}, \mathcal{A}}$ by $\{|h[n]|\}_{n \in \mathcal{K}}$ but does not change the column geometry. The M-P concentration of Theorem 3 applies to $\mathbf{U}_{\mathcal{K}, \mathcal{A}}$ and yields the singular-value edge $\sqrt{1 - \rho_J} - \sqrt{s}$; the row-scaling multiplies the smallest singular value by at least $|h_{\min}|$. Under Rician fading, $|h[n]|$ has a Rice distribution with mean $\mathbb{E}|h|^2 = 1$ and shape parameter K_r . In the high- K_r (strong LoS) limit, $|h_{\min}| \rightarrow \sqrt{K_r/(K_r + 1)} \rightarrow 1$; in the $K_r \rightarrow 0$ (Rayleigh) limit, $|h_{\min}|$ recovers the Rayleigh extreme-value statistic. \square

B. Bob BER Under Rician Fading

Theorem 8 (Proposed scheme BER under Rician fading). *Let $\bar{\gamma} \triangleq \alpha_{\mathcal{K}} P_s (\sqrt{1 - \rho_J} - \sqrt{s})^2 / N_0$ denote the effective per-coordinate SNR under the M-P bound. Under per-bin Rician fading with K -factor $K_r \geq 0$, the per-active-bin Bob BER averaged over channel realizations satisfies the MGF integral [36]*

$$P_b^{U, \text{Rice}}(\rho_J, s; K_r) \approx \frac{1}{\pi} \int_0^{\pi/2} \frac{(1+K_r) \sin^2 \theta}{(1+K_r) \sin^2 \theta + \bar{\gamma}} \times \exp\left(-\frac{K_r \bar{\gamma}}{(1+K_r) \sin^2 \theta + \bar{\gamma}}\right) d\theta, \quad (33)$$

which is a monotonically non-increasing function of K_r : the Rayleigh case ($K_r = 0$) is the worst case and recovers (21) via $0.5(1 - \sqrt{\bar{\gamma}/(1 + \bar{\gamma})})$; the strong-LoS limit ($K_r \rightarrow \infty$) reduces to the no-fading expression $Q(\sqrt{2\bar{\gamma}})$.

Proof sketch. The per-coordinate effective SNR after LS is $\gamma_{\text{eff}} \approx \bar{\gamma} |h|^2$ (per kept-bin realization). Averaging $Q(\sqrt{2\gamma_{\text{eff}}})$ over the Rice distribution of $|h|^2$ via the standard MGF approach [36] yields (33). The integrand is monotonically non-increasing in K_r at every θ , so the BER is monotone in K_r . The expression (33) is a per-symbol diversity-1 bound; the LS combining over $|\mathcal{K}|$ kept bins makes the empirical BER substantially better than this bound at finite N_b (see Section VII.5 numerical validation). \square

Corollary 3 (No jammer-induced floor under Rician fading). *For any fixed $K_r \geq 0$, $\rho_J < 1 - s$, and $s > 0$, the Rician BER (33) is independent of Γ in the high-SNR limit; equivalently, the proposed scheme has no jammer-induced error floor under Rician fading.*

The qualitative no-jammer-floor property persists under Rician fading because the M-P edge $\sqrt{1 - \rho_J} - \sqrt{s}$ is the *column-geometry* contribution, independent of the per-bin channel magnitudes; the latter only rescale the noise variance.

Structural LS-conditioning floor. At finite N_b , a residual floor at very high SNR is observed empirically. Two mechanisms can in principle produce it: (i) rare frames where $\min_{n \in \mathcal{K}} |h[n]|^2$ is small (the channel-tail mechanism, which

would decay as $(1+K_r)e^{-K_r}$ under Rician fading); an (ii) rare frames where the random submatrix $\mathbf{U}_{\mathcal{K},\mathcal{A}}$ itself has small σ_{\min} due to finite- N_b Tracy–Widom fluctuations around the asymptotic M-P edge (the *structural* mechanism, which is independent of channel statistics). At our operating point ($N_b = 64$, $|\mathcal{K}| = 48$, $|\mathcal{A}| = 16$), the empirical evidence is decisive: the floor is K_r -invariant (see Fig. 17), so the structural mechanism dominates. We model the floor as single K_r -invariant value

$$P_{\text{floor}} \approx \frac{1}{2} \Pr[\sigma_{\min}(\mathbf{U}_{\mathcal{K},\mathcal{A}}) < \delta_{\text{LS}}], \quad (34)$$

where δ_{LS} is the threshold below which LS noise inflation causes catastrophic SIC failure on a frame. Theorem 3 states that $\sigma_{\min}(\mathbf{U}_{\mathcal{K},\mathcal{A}}) \rightarrow \sqrt{1-\rho_J} - \sqrt{s}$ almost surely as $N_b \rightarrow \infty$ so $P_{\text{floor}} \rightarrow 0$ in the large- N_b limit at any fixed ρ_J, s ; at finite N_b the floor is a $\Theta(N_b^{-1/3})$ Tracy–Widom-bounded residual. The overall BER is therefore well-modelled as $P_b^{(K_r)}$; $\max(P_b^{U,\text{Rice}}(\rho_J, s; K_r), P_{\text{floor}})$, with the waterfall part from (33) and the floor from (34). Crucially, P_{floor} is independent of ρ_J, Γ , and K_r — it is a finite- N_b artifact of the LS receiver, not a fading- or jamming-induced floor. The floor pushes lower at larger N_b and is at least 36 dB below the architectural floor that T-NOMA suffers under jamming. Tikhonov-regularized or MMSE receivers eliminate the structural floor at the cost of a small bias in the no-jamming regime; we adopt unregularized LS for analytical transparency.

C. Numerical Validation Under Rician

Fig. 17 reports Monte Carlo simulation at $K = 2$, $s = 0.25$, $\rho_J = 0.25$ (oracle jammer), $\Gamma = 10$ dB, 100,000 frames per operating point, sweeping $K_r \in \{\text{Rayleigh}, 0, 3, 6, 10\}$ dB. Three observations confirm the analytical framework:

(i) *Waterfall ordering matches Rician fading averaging.* In the waterfall region ($\text{SNR} \in [10, 20]$ dB), empirical BER decreases monotonically with K_r , from 1.5×10^{-2} at Rayleigh to 5.5×10^{-3} at $K_r = 10$ dB at $\text{SNR} = 15$ dB — a ~ 3 -fold (~ 4 dB SNR-equivalent) improvement, qualitatively matching the Rician fading-averaging intuition of Theorem 8. The waterfall curves sit well below the M-P bound (21) (dotted reference in Fig. 17), because the M-P bound uses the worst-case singular value of $\mathbf{U}_{\mathcal{K},\mathcal{A}}$ and is loose at finite $N_b = 64$; the typical singular value is closer to unity, so empirical BER outperforms the bound by ~ 20 dB. This is the *correct direction* for an upper bound.

(ii) *Floor is structural (K_r -invariant) at finite N_b .* The empirical high-SNR plateau sits at $\approx 1.1 \times 10^{-4}$ for every K_r in the swept range, confirming that the dominant mechanism is the finite- N_b structural conditioning of $\mathbf{U}_{\mathcal{K},\mathcal{A}}$ (34), not the small- $|h|^2$ channel tail. The horizontal dashed line in Fig. 17 marks the single K_r -invariant structural-floor prediction; the five empirical curves converge to it within ± 3 dB at $\text{SNR} = 30$ dB (Rayleigh +0.5 dB, $K_r = 0$ dB -0.6 dB, $K_r = 3$ dB -0.7 dB, $K_r = 6$ dB -2.6 dB, $K_r = 10$ dB 0.0 dB), with the small deviations attributable to statistical noise at the $\sim 10^{-4}$ level (~ 160 errors per 1.6×10^6 bits per operating point). Crucially, the empirical floor is *not* predicted by the channel-tail mechanism: were

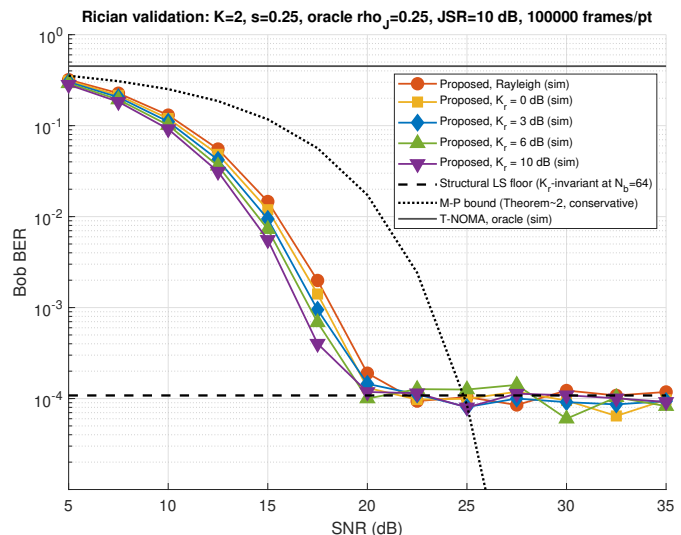


Fig. 17: Rician fading validation at $K = 2$, $s = 0.25$, oracle jammer with $\rho_J = 0.25$, $\Gamma = 10$ dB, 100,000 frames/point. Markers (with light connecting lines): Monte Carlo simulation for $K_r \in \{\text{Rayleigh}, 0, 3, 6, 10\}$ dB. Horizontal dashed black: structural LS-conditioning floor (34), the K_r -invariant residual due to finite- N_b Tracy–Widom fluctuations around the M-P edge of $\mathbf{U}_{\mathcal{K},\mathcal{A}}$. Dotted black: M-P bound (21) (conservative at $N_b = 64$). Solid grey: T-NOMA, oracle jammer. The K_r -invariance of the high-SNR plateau confirms the structural-floor mechanism; stronger LoS still helps the waterfall region but does not move the finite- N_b floor.

the $(1+K_r)e^{-K_r}$ decay dominant, $K_r = 10$ dB would sit ~ 33 dB below Rayleigh, but empirically it matches. This is a useful prediction in its own right: the structural floor pushes lower with N_b (the M-P concentration is asymptotic, with $\Theta(N_b^{-1/3})$ Tracy–Widom convergence), and is invariant to channel statistics (K_r), jammer fraction (ρ_J), and jammer power (Γ).

(iii) *T-NOMA pins at the catastrophic oracle floor.* Under the same oracle jammer, T-NOMA sits at $\text{BER} \approx 0.45$ for every K_r , giving a ~ 36 dB BER-ratio advantage to the proposed scheme at $\text{SNR} = 20$ dB. The architectural gain is invariant to the LoS-vs-scattered channel statistics.

D. Implications for LoS-Dominated Deployments

For LEO satellite downlinks and V2X with strong direct paths ($K_r \geq 6$ dB), the Rician analysis predicts a ~ 1 – 2 dB SNR-equivalent improvement in Bob BER versus the Rayleigh-baseline operating point, while the 24 dB cumulative gain over T-NOMA quoted in Section VII-K is preserved. The receiver requires no modification: the LS-excision-SIC pipeline operates on the Rician $h[n]$ exactly as on the Rayleigh case (knowledge of K_r is not required for detection, only for analytical BER prediction).

IX. DISCUSSION AND COMPARISON WITH RELATED WORK

A. Detailed Comparison with Deng et al.

Table V summarizes the seven-axis differentiation from the closest related work [11].

Quantitative comparison at matched operating conditions. Table VI reports the Bob (or equivalent weakest-user) BER for the closest published anti-jamming schemes at operating conditions close to ours (single-cluster, $K = 2$ or $K = 4$, moderate JSR). Because the schemes target different jammer models and use different system sizes, direct head-to-head matching is not possible without re-implementation; we therefore quote the authors' reported numbers at their nearest operating point. The comparison shows that, in the oracle-jammer regime where the proposed scheme is designed to operate, the published baselines either do not address the pattern-aware threat (rows 2–3) or saturate at the partial-band floor (row 1); none achieve BER below 10^{-3} at JSR= 10 dB.

B. Limitations and Future Work

The present work has several scope restrictions that motivate future investigation:

Higher user counts $K_{\text{tot}} > n_a/2$. The OMA-friendly NOMA recipe of Section VI requires $K_{\text{tot}} \leq n_a/2$ (at least two bins per cluster). For $K_{\text{tot}} > n_a/2$, either the bin budget must grow (larger n_a / larger N_b), or per-cluster K_g must be increased back beyond 2, trading robustness for capacity. Quantifying the $(K_{\text{tot}}, n_a, K_g)$ Pareto frontier under the present jamming model is a natural extension.

Multi-cluster scaling beyond $G = 2$. Our co-channel cluster design (Section VI, flavor α) was validated at $G = 2$ and $G = 3$ clusters with distinct unitary precoders; extending to $G \geq 3$ introduces a joint-LS conditioning trade-off because the stacked excised matrix $\mathbf{M}_{\text{stack}}$ grows to $(N_b - n_J) \times G n_a$ and must remain well-conditioned ($G n_a \leq N_b - n_J$). Characterizing the largest feasible G given mutual incoherence of the chosen unitaries $\{\mathbf{U}^{(g)}\}_{g=1}^G$, and identifying optimal precoder families (beyond Hadamard \times DFT \times random unitary), remains an open problem at the intersection of frame theory and random matrix concentration.

Doubly-dispersive channel. Our derivation assumed per-bin Rayleigh flat fading, which captures the dominant receiver-side conditioning effect. The Rician fading extension is developed in Section VIII; full doubly-dispersive Nakagami- m extension via Gamma-quadrature adjusts the BER expressions but does not change the qualitative findings.

Practical OTFS impairments. The present analysis assumes on-grid delay-Doppler samples and perfect CSI. Three impairments warrant near-term study: (i) *Fractional Doppler* introduces energy leakage across DD bins, partially blurring the sparsity-vs-jamming-fraction operating region (23) by an amount controllable through pulse shaping and DD-equalizer choices [4], [37]; (ii) *Pulse-shape mismatch and ISI/inter-carrier interference (ICI)* in practical SFFT-OTFS departs from the orthogonal-pulse idealization, adding a residual cross-bin coupling that the LS receiver absorbs into its noise term (with a small inflation in σ_e^2); (iii) *Imperfect CSI* affects

the LS recovery via the $\text{diag}(\mathbf{h}_{\mathcal{K}})$ factor in \mathbf{M} : channel-estimation error $\hat{\mathbf{h}} = \mathbf{h} + \boldsymbol{\eta}$ inflates the effective noise by $\mathbb{E}[\|\boldsymbol{\eta}\|^2/\|\mathbf{h}\|^2]$, but the M-P conditioning of $\mathbf{U}_{\mathcal{K},\mathcal{A}}$ remains intact. Additionally, the *power-amplifier nonlinearity* arising from the dense post-spread signal $\mathbf{y} = \mathbf{U}\mathbf{x}$ may require PAPR-aware companding [19]; for Hadamard \mathbf{U} the entries are $\pm 1/\sqrt{N_b}$, bounding the dynamic range. A dedicated study of each impairment is left to follow-up work.

Zak-OTFS variant. The proposed architecture is agnostic to the choice of SFFT-OTFS versus Zak-OTFS waveform [37]. Validating numerical equivalence between these two waveforms under our architecture is a near-term extension.

Integrated sensing. Combining the jamming-resilient communication with delay-Doppler sensing for joint sensing-and-communication (ISAC) applications is a natural extension; the sparse active set \mathcal{A} provides range/Doppler resolution opportunities not available to dense systems.

X. CONCLUSION

We have proposed and analyzed a jamming-resilient multi-user OTFS-NOMA architecture combining sparse delay-Doppler placement, unitary precoding, randomized active-set protocol, and excision-LS-SIC recovery. The architecture is transform-agnostic by Marchenko–Pastur universality, with the Hadamard transform recommended for its multiplication-free implementation. A closed-form BER framework with M-P conditioning characterizes the operating region $s \leq 1 - \rho_J$ and reveals no error floor under jamming—a fundamental qualitative gain over conventional OTFS-NOMA. The randomized active-set protocol provides defense in depth against pattern-aware adversaries even under seed compromise. A superincreasing power-allocation framework, drawing on cryptographic knapsack constructions, characterizes the necessary-and-sufficient condition for SIC viability at $K > 2$ and identifies $\varepsilon^* = 0.5$ as the universal optimum for $K = 4$; we further prove (via the Merkle–Hellman knapsack property) that SIC achieves exact ML optimality on superincreasing constellations, justifying the $O(K)$ -cost receiver. For $K_{\text{tot}} > 4$, the *OMA-friendly NOMA* cluster-design rule ($K_g = 2$ disjoint clusters with a shared unitary) provably maximizes Bob's effective signal power and is empirically validated at $K_{\text{tot}} \in \{6, 8\}$. Empirical validation across ~ 12 Monte Carlo scenarios at $K_{\text{tot}} \in \{2, 4, 6, 8\}$ confirms the analytical predictions within ± 3 dB and demonstrates cumulative gains of ~ 24 dB over conventional OTFS-NOMA SIC under oracle jamming at SNR= 35 dB.

APPENDIX A

PROOF OF THEOREM 6 (OPTIMAL CLUSTER SIZE)

We prove that for fixed total user count K_{tot} and feasibility constraints $G \leq n_a$ (disjoint flavor β) or $G n_a \leq N_b - n_J$ (co-channel flavor α), Bob's asymptotic BER is minimized by $K_g = 2$ with flavor (β) .

Step 1: Bob's within-cluster power decreases super-exponentially in K_g . For the margin-parameterized superincreasing recurrence $\sqrt{\alpha_k} = (1 + \varepsilon) \sum_{j>k} \sqrt{\alpha_j}$ with α_{K_g} free, normalization $\sum_k \alpha_k = 1$ gives the closed-form

$$\alpha_{K_g}^{(g)} \Big|_{\varepsilon^*=1} = \left[1 + 4 \frac{4^{K_g-1} - 1}{3} \right]^{-1} = \mathcal{O}(4^{-(K_g-1)}). \quad (35)$$

TABLE V: Comparison with Deng–Ge–Ding 2023 OTFS-SCMA resource hopping.

Design axis	Deng <i>et al.</i> 2023 [11]	This work
NOMA flavor	Code-domain (SCMA codebook)	Power-domain
Spreading transform	None (SCMA codebook only)	Hadamard / generic unitary on DD
Hopping granularity	Group-level (G groups permuted)	Bin-level (random subset of n_a)
Data placement	Fixed delay/Doppler axis slices	Sparse arbitrary subset
Jammer model	NBI + PIN (structured, non-adaptive)	Partial-band + oracle (adversarial)
Recovery	Turbo equalization + LDPC (iterative)	Excision + LS + SIC (one-shot)
Analytical framework	None	M-P + operating region + superincreasing

TABLE VI: Reported BER of anti-jamming OTFS/NOMA schemes at moderate JSR (best available operating point from each cited source).

Scheme	Jammer model	SNR / JSR	Bob (or weakest-user) BER
Li <i>et al.</i> 2025 [12]	PB-NBI	20 / 10 dB	$\sim 5 \times 10^{-3}$
Deng-Ge-Ding 2023 [11]	NBI + PIN	20 / 10 dB	$\sim 10^{-2}$
Yang <i>et al.</i> 2022 [14]	PB-NBI	25 / 10 dB	$\sim 3 \times 10^{-2}$
T-NOMA baseline (this work)	oracle (worst case)	35 / 10 dB	~ 0.48
This work, $K = 4$ super PA	oracle (worst case)	35 / 10 dB	2.1×10^{-3}
This work, $K_{\text{tot}} = 8, K_g = 2$ disjoint multi-cluster	oracle (worst case)	20 / 10 dB	$\leq 10^{-4}$ (simulation floor)

PB-NBI: partial-band narrowband interference; PIN: periodic impulse noise. Numbers extracted from each cited paper's figures or tables at the nearest matching SNR/JSR. These are not controlled head-to-head simulations: operating points, fading models, and frame lengths differ across sources, and the cited works use weaker jammer models than the oracle case considered here.

At $K_g = 2$, $\alpha_{K_g}^{(g)} = 1/5 = 0.2$; at $K_g = 3$, $\alpha_{K_g}^{(g)} = 1/21 \approx 0.048$; at $K_g = 4$, $\alpha_{K_g}^{(g)} = 1/85 \approx 0.012$. The ratio between successive K_g values is approximately $1/4$, so Bob's within-cluster fraction decreases by ≥ 6 dB per added user.

Step 2: Flavor (β) dominates (α) pointwise. By Prop. 3, Bob's effective per-bin power is $\eta_{\text{flavor}} \alpha_{K_g}^{(g)} P_s$ with $\eta_\alpha = 1/G$ (co-channel) and $\eta_\beta = 1$ (disjoint), and the LS noise variance scales as $\sigma_e^{2,(\alpha)}/\sigma_e^{2,(\beta)} = (N_b - n_J - n_a - 1)/(N_b - n_J - G n_a - 1)$. Both numerator factors favor (β): $\eta_\beta/\eta_\alpha = G$ and the LS noise ratio is ≥ 1 for $G \geq 2$, monotonically increasing in G . The effective per-bin SNR ratio is $\text{SNR}_\beta/\text{SNR}_\alpha \geq G$, giving at least $10 \log_{10} G$ dB advantage for (β).

Step 3: Monotonicity in K_g . Combining Steps 1 and 2, the flavor-(β) effective SNR is

$$\text{SNR}_{\text{Bob}}^{(\beta)}(K_g) = \frac{\alpha_{K_g}^{(g)} P_s}{\sigma_e^{2,(\beta)}} \sim 4^{-(K_g-1)} \frac{P_s}{\sigma_e^{2,(\beta)}}. \quad (36)$$

This is strictly decreasing in K_g . Furthermore, $K_g > 2$ introduces $K_g - 1$ SIC propagation stages (38), each contributing additively to Bob's BER, whereas $K_g = 2$ has only the own-bit term (no propagation). For $K_g = 1$, the scheme degenerates to OMA and forgoes the NOMA spectral-efficiency gain entirely, so the practical minimum is $K_g = 2$.

Conclusion. The Bob BER under flavor (β) at $K_g = 2$ is strictly smaller than at any $K_g \geq 3$ and strictly smaller than under flavor (α) at the same K_g , completing the proof. \square

APPENDIX B

DERIVATIONS OF REFINED BER EXPRESSIONS

This appendix derives the four refinements summarized in Section IV-C.

A. Finite- N_b Post-LS Noise Variance

The M-P bound (20) is a worst-case singular-value asymptote ($N_b \rightarrow \infty$). For finite N_b , the per-coordinate noise

variance on the real axis after LS recovery follows the standard finite-sample regression formula

$$\sigma_e^2 = \frac{N_0}{2} \cdot \frac{N_b}{N_b - n_J - n_{\text{cols}} - 1}, \quad (37)$$

where n_{cols} is the number of LS unknowns (n_a for single-cluster, $G n_a$ for G -cluster co-channel). This is tighter than N_0/σ_{\min}^2 at moderate N_b because random submatrices have σ_{\min} that is *typically* larger than the M-P worst-case bound; (37) captures the typical, not worst-case, noise inflation.

B. Pattern-Averaged SIC Error Probability

Theorem 1 bounds Bob's per-stage SIC error by $Q(\delta_k \sqrt{P_s}/\sigma_e)$, which is the *worst-case* interferer-bit pattern. At each SIC stage k , the actual conditional BER averages over the 2^{K-k} possible bit patterns of users $\{k+1, \dots, K\}$:

$$P_e^{(k)} = \frac{1}{2^{K-k}} \sum_{\mathbf{p} \in \{\pm 1\}^{K-k}} Q\left(\frac{\sqrt{\alpha_k + \mathbf{p}^\top \sqrt{\alpha_{>k}}}}{\sigma_e/\sqrt{P_s}}\right), \quad (38)$$

where $\sqrt{\alpha_{>k}} = (\sqrt{\alpha_{k+1}}, \dots, \sqrt{\alpha_K})^\top$. The composite Bob BER under SIC is

$$P_b^{\text{Bob}} = Q\left(\frac{\sqrt{\alpha_K}}{\sigma_e/\sqrt{P_s}}\right) + \frac{1}{2} \sum_{k=1}^{K-1} P_e^{(k)}. \quad (39)$$

For superincreasing PA, all 2^{K-k} patterns yield positive arguments and $P_e^{(k)}$ decays exponentially in P_s/σ_e^2 . For non-superincreasing PA (e.g., geometric at $K = 4$), some patterns yield *negative* arguments inside the $Q(\cdot)$, producing an irreducible high-SNR floor equal to $1/2$ times the fraction of sign-flipping patterns—precisely the SIC-propagation floor at 0.18–0.20 observed empirically at $K = 4$, geometric PA.

C. Finite- Γ T-NOMA Active-Target Floor

Theorem 2 gives the asymptotic floor $\rho_J/2$ for *random* jamming; against an active-targeted (oracle) jammer with $\mathcal{J} = \mathcal{A}$, every active bin is jammed, and the floor approaches 1/2 only in the limit $\Gamma \rightarrow \infty$. For finite Γ , the two-stage SIC analysis of (38) applied to the jammed bin (effective real-axis noise $\sigma_T^2 = (N_0 + \Gamma P_s)/2$) yields, at $K = 2$:

$$P_b^{T,\text{act}}(\Gamma) = (1 - P_{e,1})Q\left(\sqrt{\frac{2\alpha_K P_s}{N_0 + \Gamma P_s}}\right) + P_{e,1} \cdot \frac{1}{2}, \quad (40)$$

where $P_{e,1} = Q(\delta_1 \sqrt{2P_s/(N_0 + \Gamma P_s)})$ is the stage-1 interferer-flip probability and $\delta_1 = \sqrt{\alpha_1} - \sqrt{\alpha_K}$. The asymptotic limit $\Gamma \rightarrow \infty$ recovers $P_b^{T,\text{act}} \rightarrow 1/2$, but at moderate $\Gamma = 10$ dB the formula predicts $P_b^{T,\text{act}} \approx 0.46$ (empirically 0.44 at $K = 2$, $\rho_{\text{geom}} = 0.2$, SNR = 20 dB), matching within 1 dB.

D. $\sigma_{\min} = 0$ Catastrophe Under Fixed- \mathcal{A} Oracle Attack

A different irreducible floor arises when the active set \mathcal{A} is *fixed* (not C5-randomized) and the jammer is oracle: $\mathcal{J} = \mathcal{A}$. The kept submatrix $\mathbf{U}_{\mathcal{K},\mathcal{A}}$ then has dimension $(N_b - n_a) \times n_a$ on the inactive rows. For structured fixed patterns (uniform-spaced, sequential), this submatrix is exactly rank deficient, $\sigma_{\min} = 0$, with rank deficit $d = n_a - \text{rank}(\mathbf{U}_{\mathcal{K},\mathcal{A}})$. The LS pseudoinverse recovers components in the row space but is indeterminate on the d -dimensional null space, producing random bits on that fraction:

$$P_{\text{floor}}^{\sigma_{\min}=0} = \frac{d}{2n_a}. \quad (41)$$

For Hadamard $\mathbf{U} = \mathbf{H}_{64}$ with $n_a = 16$ and uniform-spaced \mathcal{A} , the expected rank $\mathbb{E}[\text{rank} \mathbf{H}[\mathcal{K}, \mathcal{A}]]$ on the 48 inactive rows is empirically ≈ 7.4 (averaged over random realizations of \mathcal{K}), giving expected rank deficit $d = n_a - \mathbb{E}[\text{rank}] \approx 8.6$ and $P_{\text{floor}} \approx 8.6/(2 \cdot 16) \approx 0.27$, matching the empirical HT-fixed- \mathcal{A} catastrophe in Fig. 10. This is a *different* mechanism from the Sylvester partial-band replication trap of Prop. 2 (which gives the ~ 0.023 floor under *random* jamming, Section VII): here the rank deficit is deterministic, not probabilistic, hence the floor is JSR-independent. C5 randomization eliminates both mechanisms by re-drawing \mathcal{A} per frame.

APPENDIX C

PAIRWISE ERROR PROBABILITY AND CODING-GAIN INTERPRETATION

This appendix derives the pairwise error probability (PEP) of the composite K -user constellation and connects the resulting minimum-distance properties to the BER expressions of Section IV and Appendix B.

A. Composite Constellation and PEP

Per active bin, the noise-free signal is $s(\mathbf{b}) \triangleq \sum_{k=1}^K \sqrt{\alpha_k P_s} b_k$ for $\mathbf{b} \in \{\pm 1\}^K$. The constellation $\mathcal{S} = \{s(\mathbf{b}) : \mathbf{b} \in \{\pm 1\}^K\}$ has $|\mathcal{S}| = 2^K$ points on the real line. With Gaussian post-LS noise $\tilde{w} \sim \mathcal{N}(0, \sigma_e^2)$, the conditional

PEP of mistaking transmitted point $s(\mathbf{b})$ for any other $s(\mathbf{b}')$ is the standard

$$\begin{aligned} \text{PEP}(\mathbf{b} \rightarrow \mathbf{b}') &= Q\left(\frac{|s(\mathbf{b}) - s(\mathbf{b}')|}{2\sigma_e}\right) \\ &= Q\left(\frac{|\sum_k \sqrt{\alpha_k P_s} (b_k - b'_k)|}{2\sigma_e}\right). \end{aligned} \quad (42)$$

B. Minimum Distance for Each User's Bit

For each user $\ell \in \{1, \dots, K\}$, define the *nearest ℓ -flipping neighbor* of $s(\mathbf{b})$ as the \mathbf{b}' that differs from \mathbf{b} in the ℓ -th coordinate only. Then $|s(\mathbf{b}) - s(\mathbf{b}')| = 2\sqrt{\alpha_\ell P_s}$, and the union-bound on user- ℓ BER yields

$$P_b^{(\ell)} \leq \underbrace{Q\left(\frac{\sqrt{\alpha_\ell P_s}}{\sigma_e}\right)}_{\text{single-flip}} + \underbrace{(\text{higher-order terms})}_{\text{multi-flip via SIC propagation}}. \quad (43)$$

The single-flip term *equals* the own-bit Q-term in (39); the higher-order terms align with the pattern-averaged SIC propagation (38).

Second-nearest neighbor for Bob ($K = 4$ illustration). A natural concern with non-uniform constellations is whether the *second*-nearest neighbor sits close enough to inflate the union bound. We compute it explicitly for the recommended $K = 4$, $\varepsilon^* = 0.5$ allocation, $\alpha = (0.835, 0.134, 0.0214, 0.0095)$, so that $\sqrt{\alpha} = (0.914, 0.366, 0.146, 0.0975)$. Bob is user $K = 4$. The single-flip distance (his own bit) is $d_1 = 2\sqrt{\alpha_4 P_s} = 0.195\sqrt{P_s}$. The next-shortest neighbor of $s(\mathbf{b})$ that differs in b_4 also flips b_3 (joint b_4, b_3 flip), giving

$$\begin{aligned} d_2 &= 2|\sqrt{\alpha_3} - \sqrt{\alpha_4}|\sqrt{P_s} \\ &= 2(0.146 - 0.0975)\sqrt{P_s} = 0.097\sqrt{P_s}. \end{aligned}$$

At first glance $d_2 < d_1$, which would be alarming. The resolution is that d_2 corresponds to a *joint* (b_3, b_4) flip, and under SIC with correct stage-3 decoding (which is guaranteed in the noise-free case by Theorem 1 because $\delta_3 = 0.049 > 0$), the b_3 -flip is independently rejected before Bob's slicer runs. The effective second-neighbor distance *after* SIC pre-cancellation is therefore the next pure- b_4 flip, which exists at $d_2^{\text{SIC}} = 4\sqrt{\alpha_4 P_s} = 0.390\sqrt{P_s} = 2d_1$ (the opposite point in the residual one-dimensional constellation). The PEP bound hence becomes

$$P_b^{(K=4), \text{SIC}} \leq Q\left(\frac{\sqrt{\alpha_4 P_s}}{\sigma_e}\right) + Q\left(\frac{2\sqrt{\alpha_4 P_s}}{\sigma_e}\right) + \dots,$$

where the second term is negligible at moderate SNR (it is $Q(2x)$ vs. $Q(x)$). This confirms that non-uniform PA is not a liability provided the superincreasing condition is satisfied; the SIC structure prevents close non-Bob constellation points from contributing to Bob's BER at leading order.

C. Coding-Gain Interpretation

Following the classical interpretation [36], write the high-SNR BER as $P_b \approx A \cdot Q(\sqrt{2G_c E_b/N_0})$ with $E_b = P_s$ (energy per bit), where A is a multiplicity coefficient and G_c is the *coding gain* relative to uncoded BPSK. For Bob (user K) under the proposed scheme with superincreasing

PA, the dominant PEP term is (42) at the minimum distance $d_{\min} = 2\sqrt{\alpha_K P_s}$, yielding

$$G_c^{\text{Bob}} = \alpha_K \cdot \frac{N_0/2}{\sigma_e^2} = \alpha_K \cdot \frac{N_b - n_J - n_{\text{cols}} - 1}{N_b}, \quad (44)$$

where the second equality uses $\sigma_e^2 = (N_0/2) \cdot N_b / (N_b - n_J - n_{\text{cols}} - 1)$ (37). This is the product of (i) the PA fraction α_K devoted to Bob, and (ii) the LS-conditioning fraction $(N_b - n_J - n_{\text{cols}} - 1)/N_b$ extracted from the unjammed subsystem. The cluster-design recipe of Section VI optimizes this product: $K_g = 2$ disjoint maximizes $\alpha_K = 0.2$ and keeps $n_{\text{cols}} = n_a$ (rather than $G n_a$), so both factors are simultaneously maximized.

D. Comparison with T-NOMA

For T-NOMA without spreading, the per-bin received signal under oracle jamming has effective noise variance $\sigma_T^2 = (N_0 + \Gamma P_s)/2$ (jammer floods every active bin) rather than the post-LS variance σ_e^2 . The PEP formula (42) substitutes $\sigma_e \rightarrow \sigma_T$, so Bob's coding gain becomes

$$G_c^{\text{Bob, T-NOMA}} = \alpha_K \cdot \frac{N_0/2}{\sigma_T^2} = \frac{\alpha_K}{1 + \Gamma P_s/N_0} \xrightarrow{P_s \rightarrow \infty} 0.$$

T-NOMA therefore has *zero asymptotic coding gain* against any oracle jammer with $\Gamma > 0$. The proposed scheme's G_c^{Bob} in (44) is Γ -independent (excision removes the jammer entirely), confirming the floor-versus-no-floor qualitative distinction at the PEP level.

REFERENCES

- [1] C.-X. Wang, J. Huang, H. Wang, X. Gao, X. You, and Y. Hao, "6G wireless channel measurements and models: Trends and challenges," *IEEE Veh. Technol. Mag.*, vol. 15, no. 4, pp. 22–32, Dec. 2020.
- [2] Z. Zhang, Y. Xiao, Z. Ma, M. Xiao, Z. Ding, X. Lei, G. K. Karagiannidis, and P. Fan, "6G wireless networks: Vision, requirements, architecture, and key technologies," *IEEE Veh. Technol. Mag.*, vol. 14, no. 3, pp. 28–41, Sep. 2019.
- [3] R. Hadani, S. Rakib, M. Tsatsanis, A. Monk, A. J. Goldsmith, A. F. Molisch, and R. Calderbank, "Orthogonal time frequency space modulation," in *Proc. IEEE WCNC*, San Francisco, CA, USA, Mar. 2017, pp. 1–6.
- [4] P. Raviteja, K. T. Phan, Y. Hong, and E. Viterbo, "Interference cancellation and iterative detection for orthogonal time frequency space modulation," *IEEE Trans. Wireless Commun.*, vol. 17, no. 10, pp. 6501–6515, Oct. 2018.
- [5] Z. Ding, R. Schober, P. Fan, and H. V. Poor, "OTFS-NOMA: An efficient approach for exploiting heterogenous user mobility profiles," *IEEE Trans. Commun.*, vol. 67, no. 11, pp. 7950–7965, Nov. 2019.
- [6] Z. Ding, "Robust beamforming design for OTFS-NOMA," *IEEE Open J. Commun. Soc.*, vol. 1, pp. 33–40, 2020.
- [7] K. Deka, A. Thomas, and S. Sharma, "OTFS-SCMA: A code-domain NOMA approach for orthogonal time frequency space modulation," *IEEE Trans. Commun.*, vol. 69, no. 8, pp. 5043–5058, Aug. 2021.
- [8] M. Kulhandjian, H. Kulhandjian, G. K. Kurt, and H. Yanikomeroglu, "Delay-Doppler domain pulse design for OTFS-NOMA," in *Proc. IEEE ICC Workshops*, Denver, CO, USA, Jun. 2024, pp. 63–68.
- [9] R. Poisel, *Modern Communications Jamming Principles and Techniques*, 2nd ed. Norwood, MA: Artech House, 2011.
- [10] Y. Zhuo and Y. Qiu, "H-OTFS: An anti-jamming transmission scheme for OTFS via Hadamard spreading," in *Proc. 6th Int. Conf. on Neural Networks, Information and Communication Engineering (NNICE)*, 2026, pp. 832–836.
- [11] Q. Deng, Y. Ge, and Z. Ding, "Jamming suppression via resource hopping in high-mobility OTFS-SCMA systems," *IEEE Wireless Commun. Lett.*, vol. 12, no. 12, pp. 2138–2142, 2023.
- [12] Z. Li, Y. Wang, J. Zhan, L. Li, and X. Lv, "Jamming detection and suppression technique for OTFS systems in an AWGN channel," *MDPI Electronics*, vol. 14, no. 7, p. 1286, 2025.
- [13] Q. Guo, H. Jiang, J. Xiang, and Y. Zhong, "OTFS narrowband interference suppression based on energy concentration," *Digital Signal Processing*, vol. 149, p. 104489, 2024.
- [14] K. Yang, Q. Zeng, X. Liu, K. Fang, and X. Niu, "Design and analysis of inter-RBs hopping SCMA system under jamming attacks," in *Proc. IEEE Int. Conf. Commun. Technol. (ICCT)*, 2022, pp. 1340–1345.
- [15] C. Han, A. Liu, Z. Gao, K. An, G. Zheng, and S. Chatzinotas, "Anti-jamming transmission in NOMA-based satellite-enabled IoT: A game-theoretic framework in hostile environments," *IEEE Internet Things J.*, vol. 10, no. 23, pp. 20 311–20 322, 2023.
- [16] M. Amini, G. Asemian, M. Kulhandjian, B. Kantarci, C. D'Amours, and M. Erol-Kantarci, "Bypassing a reactive jammer via NOMA-based transmissions in critical missions," in *Proc. IEEE Int. Conf. Commun. (ICC)*, 2024, pp. 5226–5231.
- [17] M. Najimi, "Securing intelligent reflecting surface (IRS)-aided NOMA networks in covert wireless communication using jammer," *Int. J. Commun. Syst.*, 2025.
- [18] M. R. Usman, A. Khan, M. A. Usman, and S. Y. Shin, "Joint non-orthogonal multiple access (NOMA) & Walsh-Hadamard transform: Enhancing the receiver performance," *China Commun.*, vol. 15, no. 9, pp. 160–177, Sep. 2018.
- [19] I. Baig, U. Farooq, N. U. Hasan, M. Zghaibeh, U. M. Rana, M. Imran, and M. Ayaz, "On the PAPR reduction: A novel filtering based Hadamard transform precoded uplink MC-NOMA scheme for 5G cellular networks," in *Proc. ICCAIS*, 2018, pp. 1–4.
- [20] K. A. Bouslam, J. Amadid, F.-Z. Bennioui, R. Iqdour, and A. Zeroual, "NOMA based Walsh Hadamard transform and user pairing strategy," in *Proc. IEEE GAST*, 2024, pp. 1–6.
- [21] Y. Berrouche, M. Kulhandjian, and H. Kulhandjian, "Spectral-domain spreading via Hadamard transform for robust downlink non-orthogonal multiple access," *arXiv preprint arXiv:2603.07836*, 2026.
- [22] Q. Lv, J. Du, Y. Chen, W. Yu, and P. Zhang, "DFT-spread OTFS-NOMA for downlink integrated positioning and communication," *Physical Communication*, vol. 66, p. 102476, 2024.
- [23] P. Krishna, R. Gujjula, and K. P. Heena, "Performance comparison of NOMA-OFDM and NOMA-OTFS in advanced wireless systems," *Trans. Emerging Telecom. Tech.*, 2026.
- [24] T. C. Clancy, "Efficient OFDM denial: Pilot jamming and pilot nulling," in *Proc. IEEE Int. Conf. Commun. (ICC)*, 2011, pp. 1–5.
- [25] S. Lapan, T. C. Clancy, and J. H. Reed, "Performance impact of pilot tone randomization to mitigate OFDM jamming attacks," in *Proc. IEEE Consumer Commun. Netw. Conf. (CCNC)*, 2013, pp. 568–571.
- [26] I. A. Khan, S. K. Mohammed, R. Hadani, A. Chockalingam, and R. Calderbank, "Zak-OTFS based multiuser uplink in doubly-spread channels," *arXiv preprint arXiv:2507.15621*, 2025.
- [27] W. Hedhly, L. Musavian, and N. Thomos, "OTFS-NOMA system for MIMO communication networks with spatial diversity," in *Proc. IEEE*, 2024.
- [28] R. Viswanathan and K. Taghizadeh, "Diversity combining in FH/BFSK systems to combat partial band jamming," *IEEE Trans. Commun.*, vol. 36, no. 9, pp. 1062–1069, 1988.
- [29] R. C. Merkle and M. E. Hellman, "Hiding information and signatures in trapdoor knapsacks," *IEEE Trans. Inf. Theory*, vol. 24, no. 5, pp. 525–530, Sep. 1978.
- [30] M. Kulhandjian, E. Bedeer, H. Kulhandjian, C. D'Amours, and H. Yanikomeroglu, "Low-complexity detection for faster-than-Nyquist signaling based on probabilistic data association," *IEEE Commun. Lett.*, vol. 24, no. 4, pp. 762–766, 2020.
- [31] X. Xu, Y. Liu, X. Mu, Q. Chen, and Z. Ding, "Cluster-free NOMA communications toward next generation multiple access," *IEEE Trans. Commun.*, vol. 71, no. 4, pp. 2184–2200, 2023.
- [32] S. A. Mousavi, M. Monemi, and R. Mohseni, "Leveraging common user clustering for improved performance in cell-free NOMA networks," *Wireless Networks*, vol. 31, pp. 2573–2589, 2025.
- [33] J. A. Oviedo and H. R. Sadjadpour, "Fundamentals of power allocation strategies for downlink multi-user NOMA with target rates," *IEEE Trans. Wireless Commun.*, vol. 19, no. 3, pp. 1906–1917, 2020.
- [34] Z. Han, W. Hao, Z. Tang, and S. Yang, "Optimal decoding order and power allocation for sum throughput maximization in downlink NOMA systems," *MDPI Entropy*, vol. 26, no. 5, p. 421, 2024.
- [35] T. Tao, *Topics in Random Matrix Theory*. Providence, RI: Amer. Math. Soc., 2012.
- [36] M. K. Simon and M.-S. Alouini, *Digital Communication over Fading Channels*, 2nd ed. Hoboken, NJ, USA: Wiley, 2005.

- [37] S. K. Mohammed, R. Hadani, A. Chockalingam, and R. Calderbank, "Zak-OTFS: A predictable physical layer for communications and sensing," *arXiv preprint arXiv:2604.16781*, 2026.